

## Classical and quantum periodically driven scattering in one dimension

Michael Henseler,<sup>1</sup> Thomas Dittrich,<sup>2,\*</sup> and Klaus Richter<sup>1,†</sup>

<sup>1</sup>Max-Planck-Institut für Physik komplexer Systeme, Nöthnitzer Strasse 38, 01187 Dresden, Germany

<sup>2</sup>Departamento de Física, Universidad de los Andes, A. A. 4976, Santafé de Bogotá, Colombia

(Received 8 August 2000; revised manuscript received 25 June 2001; published 25 September 2001)

Irregular scattering at harmonically driven one-dimensional potential wells is studied both on the classical and the quantum level. We show that an ac-driven single square well, and a smooth well with oscillating bottom, are sufficient to generate chaotic scattering. For a square well with oscillating bottom, we introduce the concept of pseudointegrable scattering. The quantum dynamics of these models is treated using Floquet scattering theory, which is exact for arbitrary amplitude and frequency of the driving. In the deep quantum regime, scattering is dominated by multiphoton exchanges with the driving field, leading to complex resonance structures in transmission and reflection. For strong and fast driving, the ac-driven square well develops an effective double-well potential that introduces coherent tunneling in the scattering. We identify signatures of classical chaotic scattering in a phase-space representation of the quantum dynamics.

DOI: 10.1103/PhysRevE.64.046218

PACS number(s): 05.45.Mt, 03.65.Nk, 73.21.-b

### I. INTRODUCTION

A periodic driving represents the essence of most of the experimental methods for supplying energy to a microscopic system in a coherent, easily controllable manner: For example, in quantum chemistry, molecules are steered through a predetermined reaction path by correspondingly designed laser pulses [1,2]. Similarly, in mesoscopic physics, an electronic device can be irradiated directly in the microwave-to-infrared range [3,4]. Control mechanisms closer to the repertoire of electronics are the application of an oscillating potential via a back gate, or simply of an ac voltage between the terminals of the device.

Both the chemical and the mesoscopic applications mentioned have in common that they are most adequately described in the framework of scattering theory, with a spatially localized, but periodically time-dependent scattering potential. For a molecule passing through a laser beam or an electron passing through a device with an oscillating potential, this is obvious. An ac voltage, while nonlocal in the laboratory frame, can in fact be reduced to the same scheme by a transformation originally developed to treat atoms immersed in a spatially homogeneous radiation field [5,6].

In atomic physics and in quantum chemistry, it is standard technology to drive the intensity of the radiation to values where strongly nonlinear quantum effects, such as above-threshold ionization, multiphoton excitation, and high-harmonic generation, have to be taken into account [7], and the corresponding classical dynamics is partially or totally chaotic. This is usually not the case in mesoscopic physics, where a periodic forcing is widespread [8] but predominantly remains within the regime of linear response, such as most experiments on photon-assisted tunneling [3] or ac conductance through quantum dots [4]. Accordingly, the theoretical treatment typically resorts to perturbative or related, such as

low frequency, approximations [8]. They are clearly not suitable to access the nonlinear regime where a nontrivial classical dynamics can be expected to affect the quantum-mechanical behavior.

An adequate framework to treat quantum systems, subject to periodic driving without any restriction of amplitude or frequency, is the Floquet formalism [9–11]. While it is more well known in the context of bound systems, it can in fact be generalized to scattering problems [9]. The enormous possibilities a time-dependent scattering theory, based on the Floquet approach, offers, have barely been exploited. To be sure, there exist a few recent works where it is employed to elucidate the quantum signatures of classical chaotic scattering [12,13]. There, however, the driving is chosen in the form of kicks. This facilitates numerical studies but is far from experimental reality where the driving almost exclusively is harmonic. Quantum scattering at harmonically oscillating potentials, in turn, has been studied in the Floquet formalism [14] but without considering the possibility of irregular scattering on the classical level and its quantum-mechanical consequences. A purely classical study of scattering at harmonically driven wells and barriers, on the other hand, has recently been presented in Ref. [15]. A semiclassical treatment of driven systems with emphasis on tunneling can be found in Ref. [16].

In this work we study complex scattering at harmonically oscillating potentials, both classically and quantum mechanically. We intend to demonstrate that also in mesoscopic physics, a periodic driving allows one to see quantum irregular scattering and other nonlinear phenomena in a surprisingly simple, one-dimensional setting. We devise a few models that in their spatial structure are inspired by typical layered semiconductor nanostructures, single square or smooth wells in the dimension across the layers, and which have a harmonic driving in common. The driving can be localized in the scattering region or can be spatially homogeneous like an ac voltage. For these systems, we present a detailed analysis of the classical dynamics to show that they indeed support irregular or at least pseudointegrable scattering, and exhibit a rich scenario of mixed dynamics in the transition regime.

This implies that also on the quantum level, numerical

\*Present address: Departamento de Física, Universidad Nacional, Santafé de Bogotá, Columbia.

†Present address: Institut für Theoretische Physik, Universität Regensburg, 93040 Regensburg, Germany.

work is indispensable. Besides the general advantages of the Floquet approach also for numerics, the  $(t, t')$  method [17,18] provides a well-suited tool for the treatment of a harmonic driving. We are able to evaluate, in particular, transmission and reflection probabilities for individual Floquet channels. In the deep quantum regime, we thus see non-linear effects in the form of complicated structures in transmission and reflection. They can be explained in terms of multiphoton excitations in the scattering region. Towards the semiclassical regime, we identify signatures of classical irregular scattering in quantum phase-space distributions.

We present our models in Sec. II. Section III provides details of the classical scattering in the three systems studied. The corresponding quantum dynamics is discussed, after a brief resume of classical and quantum time-dependent scattering theory, in Sec. IV. A synopsis of the various regimes covered is given in Sec. V. A selection of more technical, nevertheless important material is contained in Appendices A to E.

## II. MODELS

We focus on two different representative classes of one-dimensional time-periodic scattering systems: Systems in which the entire scattering potential is restricted to a compact interaction region, and systems in which the time-dependent part of the potential is modeled after an ac driving.

### A. Systems with local driving

If the particle experiences a non-negligible force only in a finite region of space, the concepts of scattering theory can be applied directly. On the quantum-mechanical level, the Floquet formalism allows for generalizing the Lippmann-Schwinger equations to the case of time-periodic potentials [12,19]. For one-dimensional systems, in particular, transmission and reflection probabilities can be defined independently of the phase of the driving, see Sec. IV A.

We further restrict consideration to potentials where space and time dependence factorize,

$$V(x, t) = f(x)[V_0 + V_1 g(t)] \quad (1)$$

and the time dependence is harmonic,

$$g(t) = g(t + T) = \cos \omega t, \quad \omega = 2\pi/T. \quad (2)$$

The function  $f(x)$  defines the shape of the vertically oscillating potential. The parameters  $V_0$  and  $V_1$  denote, respectively, the depth (or height) of the time-independent part of the potential and the amplitude of the oscillation. A vertically oscillating potential provides a simple model of a capacitive coupling of an ac gate voltage to the time-independent potential  $V_0 f(x)$ . The factorization of the potential enables considerable computational simplifications. Specifically, we shall choose  $f(x)$  as a square well

$$f(x) = \theta(L - |x|), \quad (3)$$

or a smooth well

$$f(x) = \frac{1}{[\cosh(x/L)]^2}. \quad (4)$$

### B. Systems with ac driving

As a model for transport experiments performed using ac voltages, we consider systems in which the particle sees an additional alternating field while moving in an otherwise static scattering potential. For the sake of simplicity we assume the driving field to be spatially homogenous. Choosing a gauge in which all forces are gradients of a scalar potential, the total time-periodic potential is given by

$$V(x, t) = V_0 f(x) - qEx \cos \omega t. \quad (5)$$

Again,  $f(x)$  defines the shape of the static potential, with strength  $V_0$ . The charge of the particle is  $q$ , and  $E$  denotes the amplitude of the ac field.

For the above potential, asymptotically free states cannot be defined in an obvious manner and scattering theory apparently does not apply directly. This difficulty is removed by the Kramers-Henneberger transformation [5]. Consider a charged particle moving in the potential (5). Outside the interaction region, the influence of the static potential  $V_0 f(x)$ , which is assumed to decay sufficiently fast, can be neglected. The particle only sees the ac field. Hence, the velocity of the particle is given by a constant plus a harmonically oscillating term. In a reference frame performing the same lateral oscillation with respect to the laboratory frame, the particle moves with a constant velocity at large distances from the scatterer, i.e., is asymptotically free. The originally static component of the potential, however, now appears to oscillate laterally.

Another alternative is to use the gauge invariance of electromagnetism in order to replace the scalar potential  $\sim x$  in Eq. (5) by a time-periodic, but spatially homogeneous vector potential. To summarize, there are three different representations—gauges—providing equivalent descriptions of the same dynamical system. The only gauge that allows for asymptotically free states is the one that renders the static scattering potential laterally oscillating. Its advantage is the direct applicability of scattering theory. The disadvantage lies in the more complicated dependence on time and position of the potential which in general prevents a factorization as in Eq. (1). The three gauges apply to the classical as well as to the quantum-mechanical description. Further details are found in Appendix A.

In the representation of a laterally oscillating potential, Eq. (5) transforms to

$$V(x, t) = V_0 f(x - \lambda \cos(\omega t)), \quad \lambda = qE/\omega^2 m. \quad (6)$$

As a specific static potential shape  $f(x)$ , we shall again consider the square well (3).

All the potentials mentioned in this section, except Eq. (6), are consistent with the general form

$$V(x, t) = V_0 f_0(x) + V_1 f_1(x) g(t), \quad (7)$$

with the spatial shapes  $f_{0,1}$  depending on  $x$  only via  $x/L$ , and  $g$  depending on time only via  $\omega t$ . Scaling all variables accordingly,

$$\tilde{x} = \frac{x}{L}, \quad \tilde{p} = \frac{p}{Lm\omega}, \quad \tilde{t} = \omega t, \quad \tilde{E} = \frac{E}{m\omega^2 L^2},$$

$$\tilde{V}_{0,1} = \frac{V_{0,1}}{m\omega^2 L^2}, \quad (8)$$

leads to the dimensionless Hamiltonian

$$\tilde{H}(\tilde{x}, \tilde{p}; \tilde{t}) = \frac{\tilde{p}^2}{2} + \tilde{V}_0 f_0(\tilde{x}) + \tilde{V}_1 f_1(\tilde{x}) g(\tilde{t}) \quad (9)$$

with only two parameters,  $\tilde{V}_0$  and  $\tilde{V}_1$ , instead of five.

We shall mainly consider models (choosing  $\tilde{V}_0$  and  $\tilde{V}_1$  accordingly) with potentials that remain attractive over the entire period of the driving. While oscillating *barriers* are of high general interest for mesoscopic physics, a single barrier does not allow for a complex classical dynamics [20]. Therefore, in the conclusions we briefly address the case of a double barrier. See also Ref. [15] for chaotic scattering at *chains* of oscillating barriers.

### III. CLASSICAL DYNAMICS

In the Hamiltonian formulation, time-dependent systems in one dimension are described by two *nonautonomous* equations of motion. Alternatively, introducing a new fictitious variable  $z = \alpha t$  and the energy  $E$  as its canonically conjugate momentum [21,22], they transform into four *autonomous* equations of motion. Thus the time dependence amounts to one additional degree of freedom (or at least one-half, if  $E$  is not considered an extra freedom), fulfilling a necessary condition for the occurrence of chaotic motion.

Classical chaotic scattering can be identified on basis of three principal diagnostics [23]: phase-space portraits, deflection functions, and dwell-time distributions. Below, we give a brief description of these criteria for the case at hand, one-dimensional time-periodic systems.

*Stroboscopic phase-space portraits* are taken at every integer multiple of the period of the driving. They correspond to defining the  $t=0 \bmod T$  hyperplanes as Poincaré surfaces of section in the extended phase space.

Of the various *deflection functions* that can be defined for one-dimensional time-periodic systems, the outgoing momentum  $p_{\text{out}}$  as a function of the incoming momentum  $p_{\text{in}}$  proved the most suitable combination for an analysis of the scattering process. It can be shown that selfsimilarity in the deflection function implies topological chaos in the dynamical flow [24]. We therefore base our classification of scattering on the presence or absence of selfsimilar regions in  $p_{\text{out}}(p_{\text{in}})$  [25].

*Dwell-time distributions* are calculated averaging over a small interval around a given incoming momentum, and over all phases of the driving. Also the nature of the decay of the dwell-time distribution for long times reflects the type of

motion within the interaction region. As a crude distinction, an exponential decay indicates a hyperbolic dynamics [26,27], while an algebraic behavior reflects integrable motion. Mixed systems typically show a crossover from exponential to algebraic decay [28]. Pseudointegrable systems also exhibit a power-law decay of their dwell-time distribution, but for different reasons and with different exponents (see Appendix B).

In the following we apply the tools introduced above to the models described in Sec. II: scattering at a vertically and laterally oscillating square well and at a smooth well.

#### A. Pseudointegrable scattering in the vertically oscillating square well

Scaled as in Eq. (8), the vertically oscillating square well takes the form

$$\tilde{V}(\tilde{x}, \tilde{t}) = (\tilde{V}_0 + \tilde{V}_1 \cos \tilde{t}) \theta(1 - |\tilde{x}|), \quad (10)$$

with  $\tilde{V}_0 < 0$  and  $\tilde{V}_1 < |\tilde{V}_0|$ . Despite the driving, the flat bottom of the potential does not allow for a change of the kinetic energy within the well. Therefore, changes of the momentum can occur only when a trajectory passes one of the steps of the potential at  $\tilde{x} = \pm 1$ , and then are discontinuous themselves. This enables us to formulate the entire scattering dynamics as a discrete map, relating successive passages across or reflections off the steps [15]: The total energy inside the well can differ by at most  $2\tilde{V}_1$ , up or down, with respect to its value upon entering the well. This may prevent an exit, resulting in specular reflection off either one of the potential steps. It can occur for an arbitrary number of times, until a potential step is overcome again and the trajectory leaves without returning. Note, however, that the times of touching or crossing the steps have no simple relation to the period  $T$  of the driving. Therefore, this map has nothing to do with the Poincaré surfaces of section at  $t_n = nT$ , underlying the stroboscopic phase-space plots.

Trajectories starting inside the well with an initial kinetic energy  $\tilde{p}^2/2 < |\tilde{V}_0| - \tilde{V}_1$  can never acquire a positive total energy. They are trapped and inaccessible from outside. The same is true of trajectories with a higher kinetic energy if the time of flight from one wall of the well to the other is an integer multiple of the period of the potential,

$$\tilde{p}_l = \frac{1}{l\pi}, \quad (11)$$

and the initial phase  $\tilde{t}_0$  fulfills  $\tilde{p}_n^2/2 + (\tilde{V}_0 + \tilde{V}_1 \cos \tilde{t}_0) < 0$  (Fig. 1). In these cases, the dynamics is identical to that inside a square well with infinitely high walls, and therefore integrable. By contrast, trajectories starting from one of the walls within the same time intervals, but with a momentum slightly different from those given in the resonance condition (11), will only stay a finite, if long, time in the interaction region. Therefore, this part of phase space is accessible to scattering trajectories. A phase-space portrait is presented in Fig. 2.

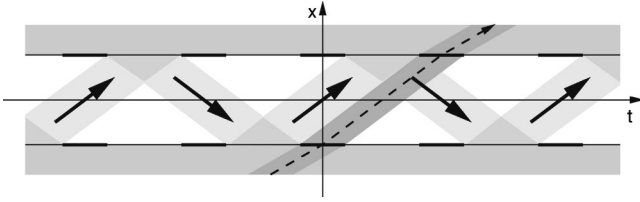


FIG. 1. Schematic space-time representation of the first ( $l=1$ ) resonant momentum, Eq. (11), in the vertically oscillating square well Eq. (10). The zigzag band consists of bound trajectories reflected between the walls of the well during closed windows of the potential (light sections of the horizontal lines representing the potential steps); a second band related to this one by parity has been omitted for clarity. The dark gray band signifies the complementary set of initial conditions, with the same resonant momentum as the trapped trajectories, but entering during an open window of the potential (bold sections of the horizontal lines) and leaving completely through the next one.

This dynamics is locally integrable, i.e., restricted to a torus. Along a manifold of measure zero, however, the torus is coupled to a different type of motion that itself is integrable again: asymptotically free scattering trajectories. Were this second part of phase space another (finite) torus, we dealt with bounded pseudointegrable motion [29]. This justifies to speak of *pseudointegrable scattering*. More precisely, unfolding configuration space inside the well along its walls and considering time as a second spatial coordinate (cf. Fig. 3), the system can be related to the unfolded barrier or graveyard billiard [30], a prototype of pseudointegrable motion.

Incoming trajectories asymptotically approaching the trapped trajectories just described form borders, each separating two topologically different types of scattering trajectories. In the deflection function (Fig. 4), these borders are visible as discontinuities. As can be seen from the resonance condition (11), they do *not* form a fractal set. This gives additional evidence that scattering at the vertically oscillating square well (10) is not chaotic. We show in Appendix B that

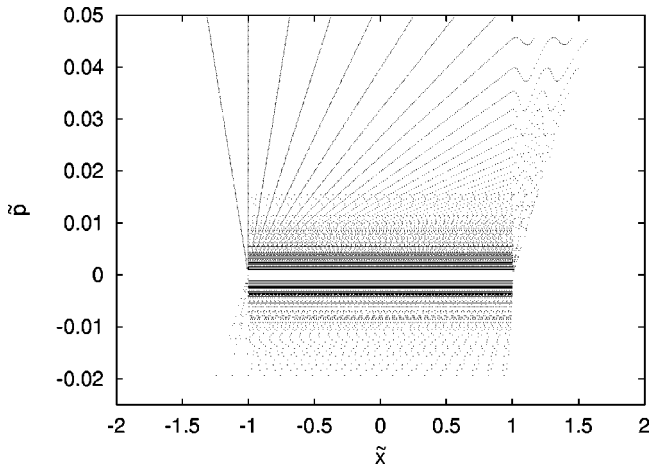


FIG. 2. Stroboscopic phase-space plot for a vertically oscillating square well, Eq. (10), with  $\tilde{V}_0 = -10^{-4}$  and  $\tilde{V}_1 = 0.999 \times 10^{-4}$ .

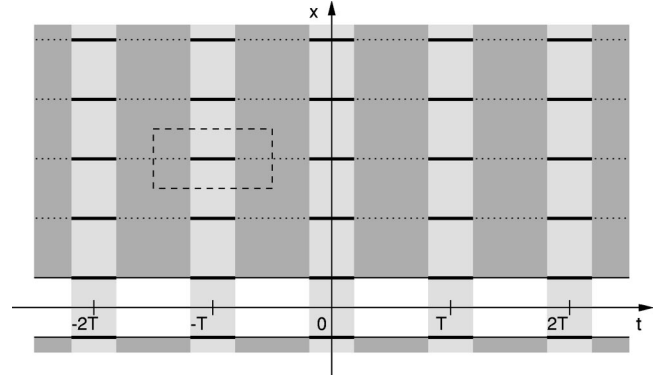


FIG. 3. Pseudointegrable scattering at the vertically oscillating square well in a schematic space-time representation. The space inside the well, with time as the horizontal coordinate, is depicted as the white horizontal rectangle. Unfolding this “billiard” along its walls (full lines) results in an infinite array of borderlines (dotted). The vertical light-shaded rectangles correspond to windows in time during which, for some arbitrary fixed kinetic energy inside the well, trajectories can escape. Where these time windows intersect the borderlines of the well (short bold lines), temporarily trapped motion within the well is connected to free scattering trajectories. A single replica of an equivalent barrier billiard is indicated by the dashed rectangle.

the long-time asymptote of the dwell-time distribution is algebraic, with an exponent  $-3$  (Fig. 5), owing to the resonance mechanism explained above. It is typical for a dynamics dominated by parabolic points [31] and has been observed in a wide variety of systems ranging from a driven square *barrier* enclosed in a potential box [32] and nonchaotic billiard chains [33] through hydrodynamical flow [34].

This phenomenon becomes more pronounced if the time windows during which nearly trapped trajectories can escape (vertical shaded rectangles in Fig. 3) are short compared to the period of the driving. That is the case, in turn, if the bottom of the barrier, at its highest position during each cycle, almost reaches the top of the well, i.e., if  $|\tilde{V}_0| - \tilde{V}_1$

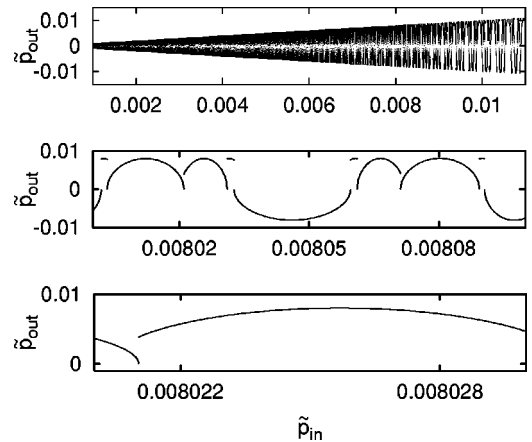


FIG. 4. Outgoing vs incoming momentum for a vertically oscillating square well, Eq. (10), with  $\tilde{V}_0 = -10^{-4}$  and  $\tilde{V}_1 = 0.999 \times 10^{-4}$ .

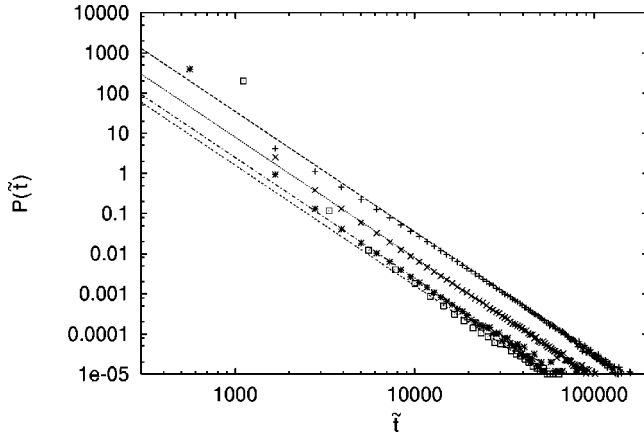


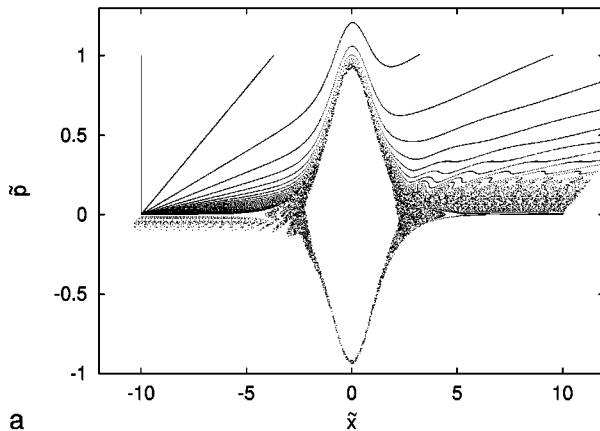
FIG. 5. Dwell-time distributions  $P(\tilde{\tau})$  (not normalized) for a vertically oscillating square well, Eq. (10), with  $\tilde{V}_0 = -10$  and  $\tilde{V}_1 = 9$  (open squares),  $\tilde{V}_1 = 9.5$  (stars),  $\tilde{V}_1 = 9.9$  (diagonal crosses),  $\tilde{V}_1 = 9.99$  (vertical crosses). The straight lines correspond to algebraic decay  $P(\tilde{\tau}) \sim \tilde{\tau}^{-3}$ .

$\ll |\tilde{V}_0|, \tilde{V}_1$ . All the data shown in the context of the vertically oscillating square well belong to this regime. The dwell-time distributions in Fig. 5, in particular, demonstrate that the agreement with the predicted power law improves upon approaching this limit. The absolute values of  $\tilde{V}_{0,1}$ , on the other hand, have a minor influence.

Scattering at the vertically oscillating square well is characterized by the absence, due to the trivial dynamics inside the well, of any mechanism that could amplify small differences in the incoming conditions to arbitrary deviations in the outgoing conditions. This is different in the following example.

### B. Weakly chaotic dynamics in the vertically oscillating smooth well

After scaling as in Eq. (8), the vertically oscillating well with the smooth static shape (4) takes the form



$$\tilde{V}(\tilde{x}, \tilde{\tau}) = \frac{(\tilde{V}_0 + \tilde{V}_1 \cos \tilde{\tau})}{(\cosh \tilde{x})^2}. \quad (12)$$

Due to the continuous nature of the potential, trajectories have to be calculated here by numerical integration of the equations of motion. Stroboscopic phase-space portraits are again defined by Poincaré surfaces of section at  $t_n = nT$ .

The nature of scattering in this case is most easily understood by considering first the motion inside the well. Due to its shape it forms an anharmonic oscillator. Switching on the driving with a small amplitude  $\tilde{V}_1 \ll |\tilde{V}_0|$  leads to resonances whenever the period of undisturbed oscillation inside the well coincides with an integer multiple of the driving period. Each of them is characterized by a chain of alternating elliptic and hyperbolic periodic points, embedded in a chaotic layer. Since the potential is not binding, however, there must be an uppermost resonance, coupled to asymptotically free trajectories. The generic global structure of phase space in this system therefore consists of three parts: Regular scattering trajectories at high energies, an intermediate region of chaotic scattering at low but positive energies, and a mixed Kol'mogorov-Arnol'd-Moser(KAM)-type region of bound motion inside the well.

This generic structure is exemplified by the phase-space portraits in Fig. 6. Panel (a) shows the scattering part of phase space, with regular trajectories at high  $|\tilde{p}|$ , and chaotic motion reaching into the asymptotic regions for small momenta. The white area of bound motion inaccessible from outside is filled in panel (b). It exhibits the typical KAM structure of interspersed tori and chaotic layers.

The conclusion that scattering at the potential (12) is chaotic already for small driving amplitudes is confirmed by the deflection functions presented in Fig. 7. Two successive magnifications clearly demonstrate their self-similarity.

Figures 8 and 9 are devoted to the extreme case that the well disappears once per period of the driving,  $\tilde{V}_1 = |\tilde{V}_0|$ . Foreseeably, the relative size of the region of chaotic scattering has increased dramatically [Fig. 8(a)]. Still, a small island of inaccessible regular motion remains near the bot-

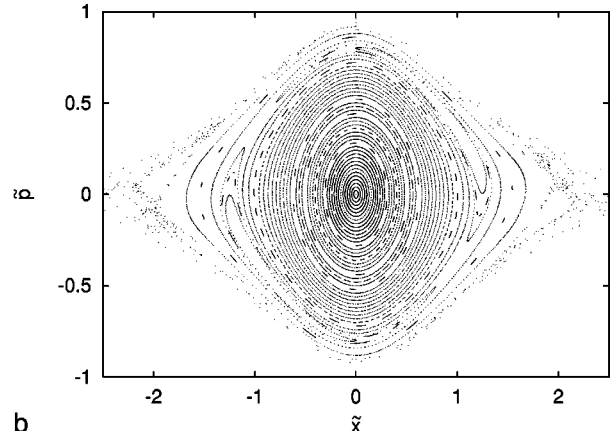


FIG. 6. Stroboscopic phase-space plots for a vertically oscillating smooth well, Eq. (12), with  $\tilde{V}_0 = -4/9$  and  $\tilde{V}_1 = 10^{-2}|\tilde{V}_0|$ . Panel (a) shows scattering trajectories, coming in from the left, panel (b) mostly bound trajectories starting at  $\tilde{x}_0 = 0$  with phase  $\tilde{\tau}_0 = \pi/2$ .

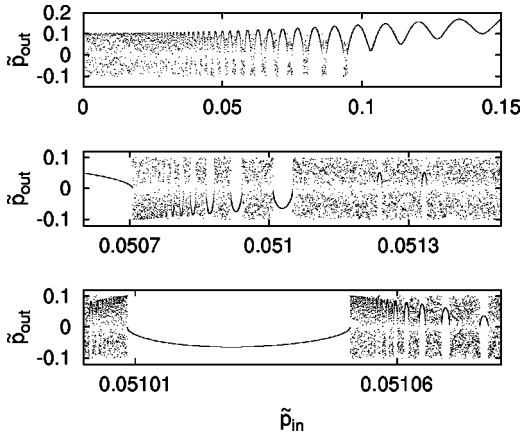


FIG. 7. Outgoing vs incoming momentum for a vertically oscillating smooth well, Eq. (12), with  $\tilde{V}_0 = -4/9$  and  $\tilde{V}_1 = 10^{-2}|\tilde{V}_0|$ . Lower panels are successive magnifications of the uppermost one.

tom of the well. Numerical evidence demonstrates that this central island persists even for values of  $\tilde{V}_1 = |\tilde{V}_0|$  orders of magnitude higher than the ones underlying the data shown. The deflection function [Fig. 8(b)] is less regular in the small-scale details than in the case of weak driving, Fig. 7, but evidently remains self-similar. The dwell-time distribution, Fig. 9, decays algebraically as expected for a system with mixed, KAM-type dynamics. However, it exhibits a very well-defined crossover, at  $\tilde{t} \approx 2.5 \times 10^{19}$ , from a slow decay  $\sim \tilde{t}^{-0.32}$  to a faster decay  $\sim \tilde{t}^{-1.21}$ . While it is clear that, in order that the distribution be normalizable, the slow decay  $\sim \tilde{t}^{-0.32}$  cannot persist to arbitrarily long times, the mechanism underlying this crossover remains open.

### C. Mixed (regular and chaotic) scattering in the laterally oscillating square well

In the case of the laterally oscillating square well, as it emerges by a Kramers-Henneberger transformation from an ac-driven well, the two respective strength parameters of the

static and the oscillating components of the potential have quite different interpretations: The oscillation amplitude now is a length, the maximum lateral shift of the well with respect to its value at rest. In dimensionless units [see Eq. (8)] the potential reads

$$\tilde{V}(\tilde{x}, \tilde{t}) = \tilde{V} \theta(1 - |\tilde{x} - \tilde{\lambda} \cos \tilde{t}|). \quad (13)$$

In particular,

$$\tilde{\lambda} = \frac{qE}{mL\omega^2} \quad (14)$$

denotes the amplitude of the lateral oscillation in terms of the electrical field strength  $E$ , charge  $q$ , frequency  $\omega$ , and total width  $2L$  of the well in unscaled units. The interaction region is sharply defined here, given by the interval  $|\tilde{x}| \leq 1 + \tilde{\lambda}$ .

As in the case of the vertically oscillating square well, there are here two independent ways of formulating the dynamics as a discrete map, defining Poincaré surfaces of section either at equidistant times  $t_n = nT$  or at the steps of the potential. The second option is better suited as a basis for a numerical calculation of trajectories. Due to the time dependence of the step position, the resulting map is quite elaborate here; we derive it in Appendix C.

A first image of the scattering at the laterally oscillating square well is obtained again by considering time as a spatial coordinate. This system thus becomes a billiard with rippled walls (Tennyson billiard [35]), see Fig. 10. The rippled-wall billiard is known to exhibit a mixed dynamics. It gives rise to an infinite set of unstable periodic orbits. The simplest and most prominent of them that can be transferred to the present case is the one connecting subsequent *convex* extrema (inner turning points) of the walls on alternating sides (cf. Fig. 10), of scaled period  $2\pi$ . At the same time, there is a complementary set of stable periodic orbits surrounded by regular islands, inaccessible from outside. The simplest one of them connects subsequent *concave* extrema (outer turning points)

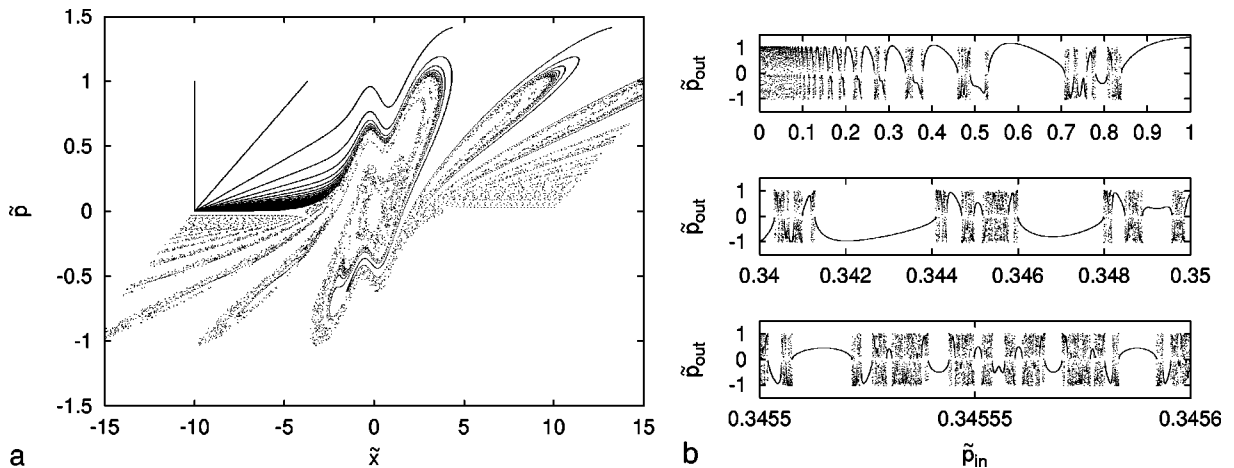


FIG. 8. Stroboscopic phase-space plot (a) and outgoing vs incoming momentum (b), for a vertically oscillating smooth well, Eq. (12), with  $-\tilde{V}_0 = \tilde{V}_1 = 4/9$ . In (b), lower panels are successive magnifications of the uppermost one.

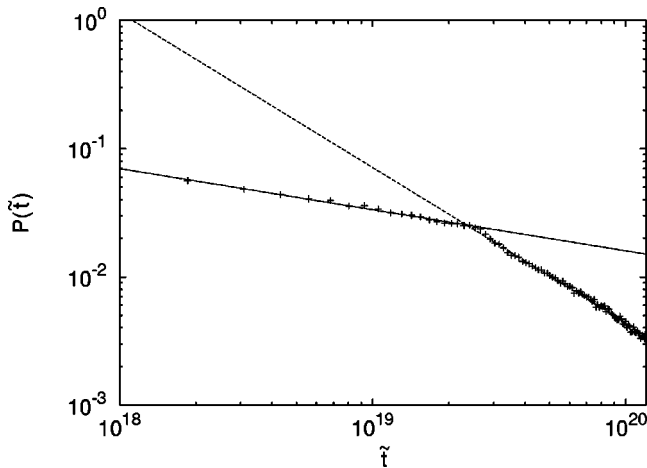


FIG. 9. Dwell-time distribution  $P(\tilde{t})$  (not normalized) for a vertically oscillating smooth well, Eq. (12), with  $-\tilde{V}_0 = \tilde{V}_1 = 5$ . The straight lines correspond to algebraic decays  $P(\tilde{t}) \sim \tilde{t}^{-0.32}$  (full line) and  $\sim \tilde{t}^{-1.21}$  (dashed).

of the walls on alternating sides (cf. Fig. 10). Taking a finite depth of the potential into account, the rippled-wall billiard also serves as a model for a phenomenon that cannot occur in a vertically oscillating well: A trajectory that has already escaped from the well, but not from the interaction region, can be ‘‘overtaken’’ by the moving wall and thus be recaptured (see leftmost orbit in Fig. 10).

Another closely related system is the Fermi accelerator [36,37]. It arises as the limit of an infinitely deep well for the present model. Also this comparison lets us expect a mixed dynamics in the laterally oscillating square well. Moreover it suggests that, in contrast to the vertically oscillating smooth well, the motion will be *more* chaotic near the bottom of the well, i.e., at low energies.

Various regimes can be distinguished, both with respect to the amplitude and the frequency of the driving, that show different types of scattering:

The relevant characteristic time scales for the scattering at oscillating potential wells are, on the one hand, the period  $T = 2\pi/\omega$  of the driving, and on the other hand, a typical time  $t_{\text{pas}}$  spent in the scattering region. A crude classical estimate of this time is the duration  $4mL/p$  of one round trip through the well, at the maximum kinetic energy  $p^2/(2m) = |V_0|$  in the well, i.e.,  $t_{\text{pas}} = 4L\sqrt{m/2|V_0|}$ . In dimensionless units [Eq. (8)],  $\tilde{T} = 2\pi$  and  $\tilde{t}_{\text{pas}} = 2\sqrt{2/|\tilde{V}_0|}$ .

If these time scales are sufficiently different, the oscillating potential can be reduced to an effective static potential. This is the case in the adiabatic limit  $T \gg t_{\text{pas}}$  and in the diabatic limit  $T \ll t_{\text{pas}}$ . In terms of the scaled parameters, they correspond to  $\tilde{V}_0 \gg 2/\pi^2$  and  $\tilde{V}_0 \ll 2/\pi^2$ , respectively. The system is then essentially one dimensional again and thus integrable. In the adiabatic case, the effective potential is the square well in its instantaneous position, in the diabatic case it is the time average of the oscillating well. The latter will be discussed below.

A nontrivial dynamics arises only if  $T$  and  $t_{\text{pas}}$  are com-

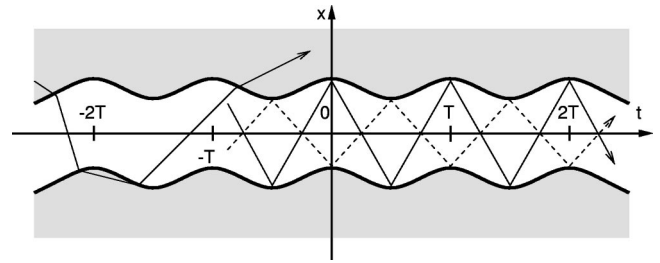


FIG. 10. Scattering at the laterally oscillating square well, in a schematic space-time representation. The white central ‘‘channel’’ is the oscillating well, its walls being indicated by bold lines. The leftmost trajectory (full line) exemplifies a process of transmission and subsequent recapture (just outside the lower wall). The full line on the right-hand side is a stable periodic orbit connecting outer turning points of the wall, the dashed line connecting inner turning points is an unstable periodic orbit.

parable ( $|\tilde{V}_0| \lesssim 1$ ). It then further depends on the amplitude  $\tilde{\lambda}$ . For small  $\tilde{\lambda}$ , phase space is mixed. For sufficiently strong driving  $\tilde{\lambda} \gg 1$ , however, all the stable periodic orbits are destroyed since even the most stable one (see Fig. 10) would intersect the moving walls at least once. Comparing to the Fermi accelerator, this corresponds to the chaotic region found at low energies [36]. It reaches out to beyond the edges of the potential steps, where in the present case it couples to asymptotically free trajectories. In this limit, the scattering at the laterally oscillating square well becomes purely chaotic, except for high-energy scattering trajectories that pass over the well without feeling it.

In the following, we illustrate some of these regimes by numerical data. Figure 11(a) is a phase-space portrait at weak driving  $\tilde{\lambda} = 0.1$ . The dominating feature is a large regular island. Its center at  $\tilde{x} = 0$  and  $\tilde{p} \approx 0.7$  corresponds to the stable periodic orbit between the outer turning points of the walls, described above. A similar unstable orbit between the inner turning points, at a smaller, negative momentum, is embedded in the large chaotic area. The adjacent regular regions consist of trajectories that are inaccessible from outside and bounce between the walls of the well, as in the Fermi accelerator. The separatrices forming the boundary towards the scattering trajectories at high positive and negative momenta are indicated by bold lines. At stronger driving,  $\tilde{\lambda} = 1.6$  [Fig. 11(b)] [38], the low-energy part of the interaction region has turned completely chaotic. The prominent regular island of the former case has disappeared, as have the separatrices between the chaotic region and the fast scattering trajectories.

The corresponding deflection functions (Fig. 12) and dwell-time distributions (Fig. 13) allow for the same conclusions. Both deflection functions shown are self-similar, but the one for stronger driving, Fig. 12(b), is less regular and shows a larger measure of chaotic sections. The dwell-time distribution for the case with mixed dynamics, Fig. 13(a), is characterized by a crossover from exponential to algebraic decay, with exponent  $-2.24$ , while in the fully chaotic case, Fig. 13(b) [38], it is purely exponential.

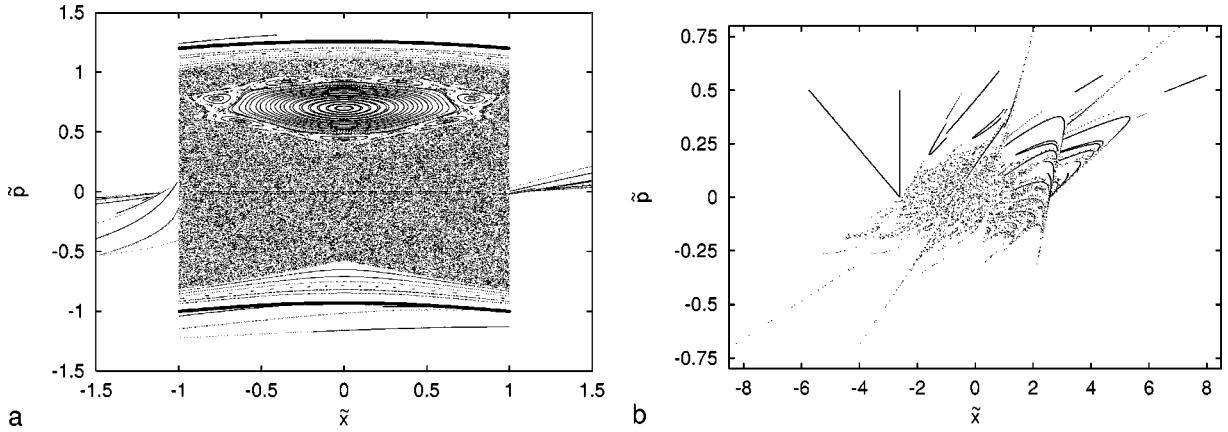


FIG. 11. Stroboscopic phase-space plots for a laterally oscillating square well, Eq. (13), with  $\tilde{V}_0 = -0.75$  and  $\tilde{\lambda} = 0.1$  (a),  $\tilde{V}_0 = -0.04$  and  $\tilde{\lambda} = 1.6$  (b). The bold lines in panel (a) are the separatrices between stable bound motion inside the well and scattering trajectories.

In the diabatic limit,  $\omega \rightarrow \infty$  or  $\tilde{V}_0 \rightarrow 0$  (in dimensionless units), the effective static potential is given by the average over a period of the driving of the time-dependent one,

$$V_{\text{eff}}(x) = \frac{1}{T} \int_0^T dt V(x, t). \quad (15)$$

This time-averaged potential is different from any instantaneous shape of the potential (13). In particular, if the ampli-

tude of the driving is smaller than the width of the well,  $\tilde{\lambda} \leq 1$ ,

$$\bar{V}(\tilde{x}) = -\frac{\tilde{V}}{\pi} \times \begin{cases} \arccos[-(1 \pm \tilde{x})/\tilde{\lambda}], & |\tilde{x} \pm 1| \leq \tilde{\lambda}, \\ \pi, & |\tilde{x}| \leq 1 - \tilde{\lambda}, \\ 0, & \text{else,} \end{cases} \quad (16)$$

while in the opposite case,  $\tilde{\lambda} > 1$ ,

$$\bar{V}(\tilde{x}) = -\frac{\tilde{V}}{\pi} \times \begin{cases} \arccos[-(1 \pm \tilde{x})/\tilde{\lambda}], & |\tilde{x} \pm \tilde{\lambda}| \leq 1, \\ \arccos[-(1 + \tilde{x})/\tilde{\lambda}] + \arccos[-(1 - \tilde{x})/\tilde{\lambda}], & |\tilde{x}| \leq \tilde{\lambda} - 1, \\ 0, & \text{else.} \end{cases} \quad (17)$$

See Appendix D for a derivation. In this latter case of strong driving, the effective potential develops a central *maximum*. The reason is that the oscillation ranges of the walls then overlap near the origin. As a result, the potential there takes on its higher value, zero, for a longer time within each period than further outside. In effect, the potential assumes the form of a double well, cf. Fig. 14. This requires that the square well slows down near the turning points of its lateral oscillation as it does for a harmonic driving; by contrast, to a piecewise linear (sawtooth) or impulsive (delta) time dependence, this does not apply. A situation converse to the one just described occurs for a laterally oscillating square *barrier* (turn Fig. 14 upside down): It develops a central *minimum* if the amplitude of the oscillation exceeds the barrier width [14].

Figure 15 is a phase-space portrait of the laterally oscillating square well in its diabatic limit. Apparently, there are no more chaotic areas present. The motion along the locally regular-looking structures in the center is not integrable, either: Some of the incoming trajectories may loose sufficient

energy to the oscillating barrier walls that they remain trapped for an appreciable time. As long as they remain within one of the three smooth sections of the effective potential, cf. Fig. 14, they are confined to some torus of the corresponding static system. At the cusps of the potential, at  $\tilde{x} = \pm(\tilde{\lambda} - 1)$ , however, the diabatic approximation is no longer valid since there, a series of rapid collisions with the walls may abruptly cease or set in. Thus, the jump onto a particular torus on which the trajectory continues on the far side of the cusp, can be considered a random event that depends sensitively on the phase of the oscillation in the moment of passing the cusp. A similar consideration applies to the events of entering or leaving the central phase-space region at  $\tilde{x} = \pm(\tilde{\lambda} + 1)$ .

As these erratic jumps maintain a rest of chaoticity of the motion, the concept of pseudointegrability does not apply here, either. The most closely related case to compare with is the return to integrability, in the limit of strong field, of billiards that are rendered chaotic by the presence of a magnetic field [39]. In that limit, the Larmor radius becomes so

small that they creep in an integrable manner along boundary sections with small curvature, but pass through chaotic episodes where the radius is of the order of the Larmor radius or below, specifically at cusps of the boundary.

The peculiar position of this type of motion between chaotic and regular is further illustrated by the deflection functions, Fig. 16(a), that exhibit accumulation points of singularities but no true self-similarity, and by the dwell-time distribution, Fig. 16(b). It falls off algebraically for long times, but exceedingly rapidly, with an exponent  $-7.64$  for this particular parameter set.

## IV. QUANTUM DYNAMICS

### A. Quantum scattering theory for time-periodic systems

Most textbooks on quantum mechanics (such as Ref. [40]) include an introduction to the theory of scattering at time-independent potentials. Time-dependent scattering, however, is not usually considered (see, for example, Ref. [41]), even though it is relevant for numerous branches of physics. A few articles deal with the generalization of time-independent scattering theory to time-periodic systems. In Ref. [9], the existence of wave operators in time-periodic scattering systems was studied. The concept of an extended Hilbert space (see, for example, Refs. [21,22]) is used in Ref. [42] for atoms in strong light fields and in Ref. [17] to describe multiphoton ionization and dissociation. The Born series is generalized in Ref. [43] to the case of time-periodic scattering systems, the low- and high-frequency limits of this theory are considered in Ref. [44]. Another cornerstone of scattering theory, the Lippmann-Schwinger equations, has been extended to periodically *kicked* potentials [12]. It can be further generalized to potentials with a periodic, but otherwise arbitrary time dependence [19,45].

We assume in the following that the time dependence of the potential is restricted to a compact scattering region. As in the time-independent case, the  $S$  matrix for a time-periodic potential then transforms an incoming asymptotic free state into an outgoing one,

$$|\psi_{\text{out}}\rangle = S|\psi_{\text{in}}\rangle. \quad (18)$$

The state vectors are taken in the Schrödinger picture and refer to the *same* time  $t_0=0$ . The time evolution of the asymptotic free states is governed by  $U_0(t) = \exp(-iH_0t/\hbar)$ , where  $H_0$  denotes the time-independent, asymptotic component of the Hamiltonian. The  $S$  matrix, by contrast, depends on the full, periodically driven Hamiltonian and in general, does not commute with  $U_0(t)$ . Therefore, a shift in the reference time  $t_0$  in Eq. (18) generally leads to a *different*  $S$  matrix,

$$\tilde{S} = U_0(t_0)S U_0^\dagger(t_0). \quad (19)$$

Only for  $t_0 = nT$ , where  $T$  is the period of the driving, we have  $\tilde{S} = S$ , as follows from  $U_0(nT) = u_0^n$ , with  $u_0 = U_0(T)$ , and the conservation of quasienergy,  $[S, u_0] = 0$ . As  $S$  and  $\tilde{S}$  are related by a unitary transformation, they are isospectral, i.e., have the same poles leading to the same resonances and associated widths.

The fact that time-periodic systems are described by a discrete dynamical group, generated by the Floquet operator, leads to the characteristics of the scattering process summarized in Table I.

In one dimension, total and partial transmission and reflection probabilities can be defined by a straightforward generalization of the corresponding concepts for time-independent potentials. We define the *partial transmission*  $T_l(E)$  [*reflection*  $R_l(E)$ ] to be the ratio of the transmitted (reflected) outgoing flux with energy  $E' = E + \hbar\omega$  to the total incoming flux (with energy  $E$ ). The *total transmission (reflection)* is given by the sum over all the corresponding partial probabilities,

$$T_{\text{tot}}(E) = \sum_{l=-\infty}^{\infty} T_l(E), \quad R_{\text{tot}}(E) = \sum_{l=-\infty}^{\infty} R_l(E), \quad (20)$$

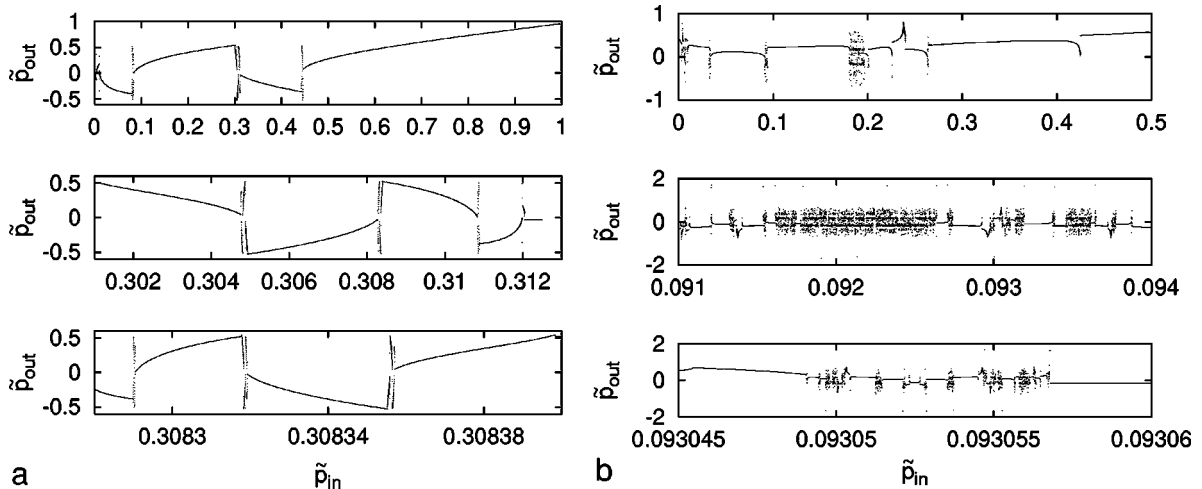


FIG. 12. Outgoing vs incoming momentum for a laterally oscillating square well, Eq. (13), at the same parameter values as in panels (a) and (b) of Fig. 11. Lower panels are successive magnifications of the respective uppermost ones.

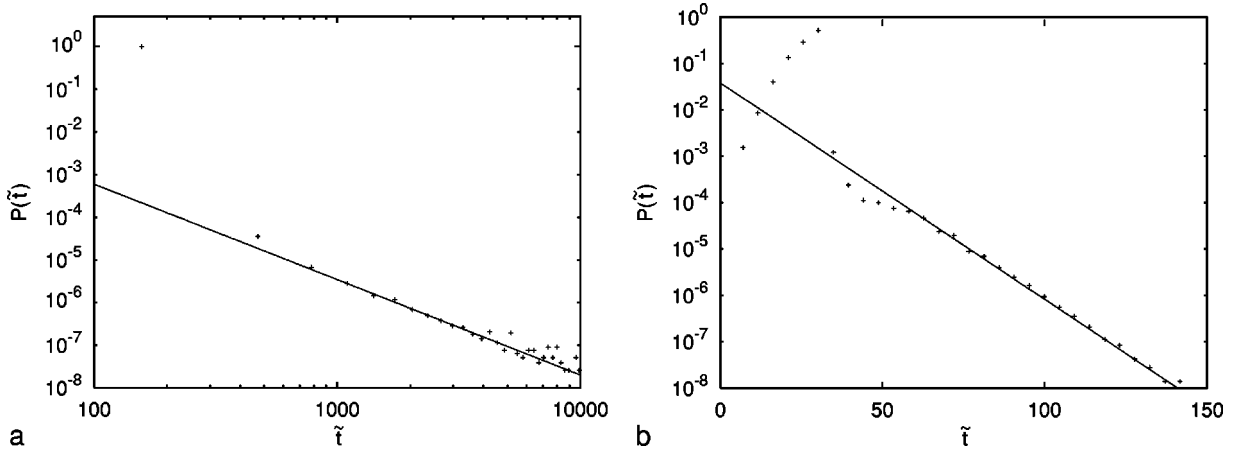


FIG. 13. Dwell-time distributions  $P(\tilde{t})$  (not normalized) for a laterally oscillating square well, Eq. (13), at the same parameter values as in panels (a) and (b) of Fig. 11. The straight line in panel (a) corresponds to an algebraic decay  $P(\tilde{t}) \sim \tilde{t}^{-2.24}$ , and that in panel (b) to an exponential decay.

where we set  $T_l(E) = R_l(E) = 0$  for  $E' = E + l\hbar\omega < 0$ . These definitions and unitarity of the  $S$  matrix ensure that  $T_{\text{tot}}(E) + R_{\text{tot}}(E) = 1$  for all positive energies  $E$ .

Transmission and reflection probabilities can be expressed in terms of the  $S$  matrix. It is defined with respect to flux-normalized incoming and outgoing asymptotic plane wave states of the form

$$\langle x | \psi_{\epsilon, n}^{0\pm} \rangle = \left( \frac{m}{2\pi\hbar^2 k_n(\epsilon)} \right)^{1/2} e^{\pm i k_n(\epsilon)x}, \quad (21)$$

where  $k_n(\epsilon) = \sqrt{2m(\epsilon + n\hbar\omega)/\hbar}$  and  $\epsilon$  is the quasienergy. This insures unitarity of the  $S$  matrix in the multichannel case we are dealing with [46]. The  $S$  matrix is given by

$$\langle \psi_{\epsilon, n}^{0\pm} | S | \psi_{\epsilon', n'}^{0\mp} \rangle = S_{n, n'}^{\pm\mp}(\epsilon) \delta(\epsilon - \epsilon'). \quad (22)$$

For reflection-symmetric potentials,  $V(-x, t) = V(x, t)$ , the four blocks  $S^{\pm\pm}$  of the  $S$  matrix reduce to two,

$$S_{n, n'}^{+\mp}(\epsilon) = S_{n, n'}^{-\pm}(\epsilon) \equiv S_{n, n'}^{\pm}(\epsilon). \quad (23)$$

The partial transmission and reflection probabilities are then given by

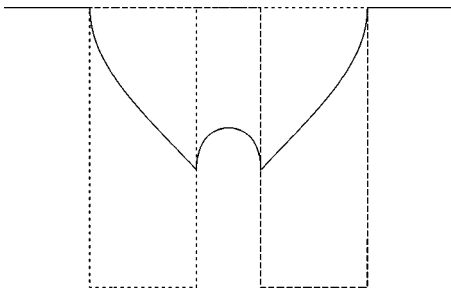


FIG. 14. Time-averaged potential (full line) and instantaneous potential at the turning points (dashed) of the laterally oscillating square well, Eq. (13), for  $\tilde{\lambda} > 1$ .

$$T_{n-n'}(\epsilon + n'\hbar\omega) = |S_{n, n'}^+(\epsilon)|^2, \quad (24)$$

$$R_{n-n'}(\epsilon + n'\hbar\omega) = |S_{n, n'}^-(\epsilon)|^2. \quad (25)$$

Depending only on  $|S_{n, n'}^{\pm}|^2$ , they are *independent* of the choice of  $t_0$  in Eq. (19).

## B. Computational procedure

All the numerical results presented in the following are based on the numerical solution of the time-dependent Schrödinger equation by propagation of wave packets, taking advantage of the enormous simplifications that result if the time evolution is only monitored stroboscopically at discrete  $t_n = nT$ . It then suffices to calculate the Floquet operator  $U(T, 0)$  once and apply it iteratively. We obtain  $U(T, 0)$  using the  $(t, t')$  method [17], a formulation of Floquet theory

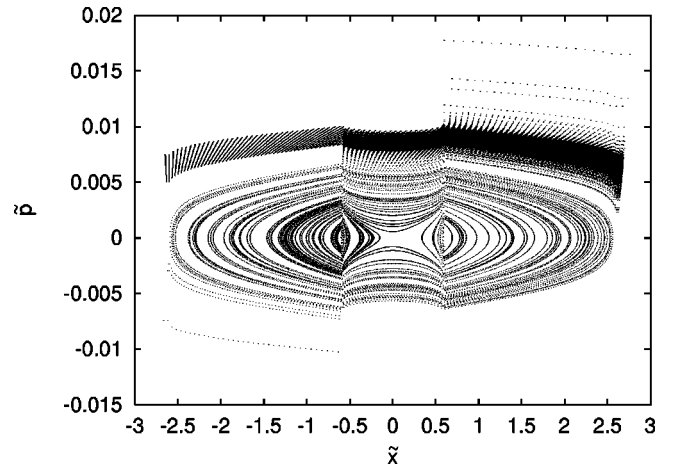


FIG. 15. Stroboscopic phase-space plot for a laterally oscillating square well, Eq. (13), with  $\tilde{V}_0 = -4 \times 10^{-5}$  and  $\tilde{\lambda} = 1.6$ .

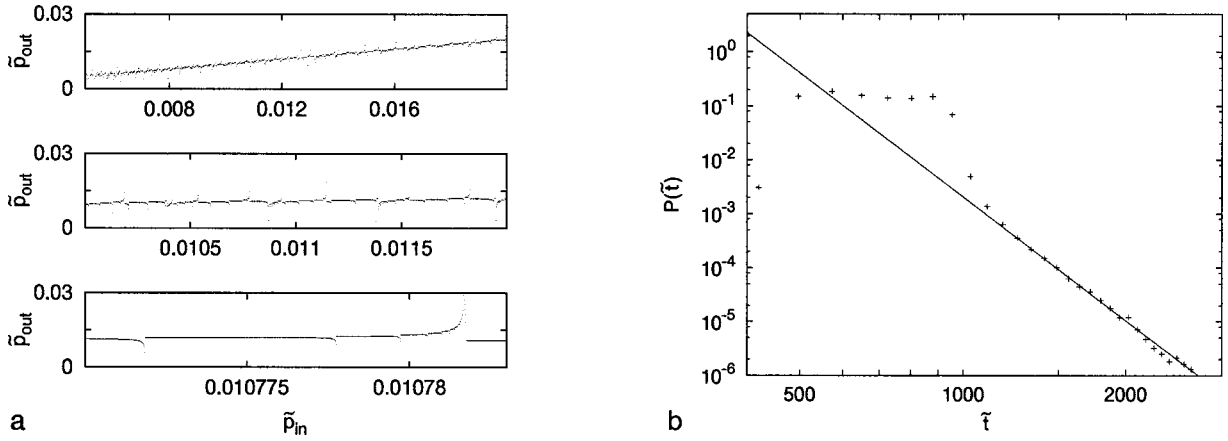


FIG. 16. Outgoing vs incoming momentum (a) and dwell-time distribution  $P(\tilde{\tau})$  [not normalized, panel (b)] for a laterally oscillating square well, Eq. (13), at the same parameter values as in Fig. 15. The straight line in (b) corresponds to an algebraic decay  $P(\tilde{\tau}) \sim \tilde{\tau}^{-7.64}$ .

that is particularly well adapted to harmonic forms of the driving. It is most efficient if the time-periodic Hamiltonian,

$$H(p, x; t) = \frac{p^2}{2m} + V(x, t) = \sum_{m=-\infty}^{\infty} H_m(p, x) e^{im\omega t}, \quad (26)$$

has only a small number of nonvanishing Fourier components  $H_m$  [17,45]. For systems with a locally confined driving, Eq. (1), where the only nonzero components are those with  $m=0, \pm 1$ , the  $(t, t')$  method works optimally.

In ac-driven systems described by the potential (5), a representation that allows for asymptotically free states is reached by performing a Kramers-Henneberger transformation, see Appendix A. The time-dependent scattering theory sketched in Sec. IV A then applies directly. The transformation, however, destroys the factorization of the potential into separate space and time dependences, see Eq. (6). As a result, the discontinuities of the potential characterizing a square well carry over to the time dependence, leading to an exceedingly slow decay  $\|H_m\| \sim 1/|m|$ , as shown in Appendix D (see also Ref. [14]). This problem is circumvented by calculating the Floquet operator in the *momentum gauge*, see Appendix A 1, where the time dependence is deferred to a vector potential appearing only in the kinetic energy. In this gauge the eigenfunctions of the kinetic energy, and thus the asymptotic states, are plane waves with a time-periodic phase factor, known as Volkov states [47]. In order to perform the stroboscopic wave-packet propagation, where time-independent asymptotic states are required, one transforms the Floquet operator from the momentum to the acceleration gauge, see Appendix A 2.

Besides the numerical calculation of transmission and reflection probabilities,  $T_l(E)$  and  $R_l(E)$ , it has proven useful to consider a heuristic dwell time in units of the period  $T$ ,

$$W(E; \omega) \sim \sum_{j=0}^{\infty} \int_{-\Lambda/2}^{\Lambda/2} dx |\psi(x, jT)|^2, \quad (27)$$

where  $\Lambda$  denotes the width of the scattering region.  $W(E; \omega)$

is distinct from the Wigner delay time, but can be readily obtained from the stroboscopic time evolution of wave packets.

### C. Effective potential and multiphoton processes

We begin the discussion of quantum scattering in our models with the deep quantum regime, dominated by isolated resonances with a mean separation larger than their width. In the context of driven scattering where no energy spectrum proper exists, the concept of resonances ought to be made more precise. It here refers to quasibound Floquet states, i.e., states with a long life time within the scattering region. It is easier to understand their existence returning for a moment to the more familiar view of a static potential plus a driving field: The potential well accommodates a finite number of bound states—in the adiabatic and diabatic limits, they are approximately given by the eigenstates of the effective static potential—which become accessible from outside by a loss or gain of photons of the driving field. Resonances associated with a Floquet state with quasienergy  $\epsilon_\alpha$  are thus expected in the vicinity of incoming energies

$$E_{\text{in}}(\alpha, n_{\text{in}}) = \epsilon_\alpha + n_{\text{in}} \hbar \omega, \quad (28)$$

TABLE I. Comparison of time-independent and time-periodic scattering systems

Time independent scattering systems	Time periodic scattering systems
Energy conserved	Quasienergy conserved
$S$ matrix: $S_{\mu, \nu}$ $\mu, \nu$ : scattering channels	$S$ matrix: $S_{\mu, m; \nu, n}$ $\mu, \nu$ : scattering channels $m, n$ : Floquet channels
Incoming and outgoing energies $E_{\text{out}} = E_{\text{in}}$	Incoming and outgoing energies $E_{\text{out}} = E_{\text{in}} + l \hbar \omega$ $l = m - n$ integer $\omega = 2\pi/T$ : driving frequency

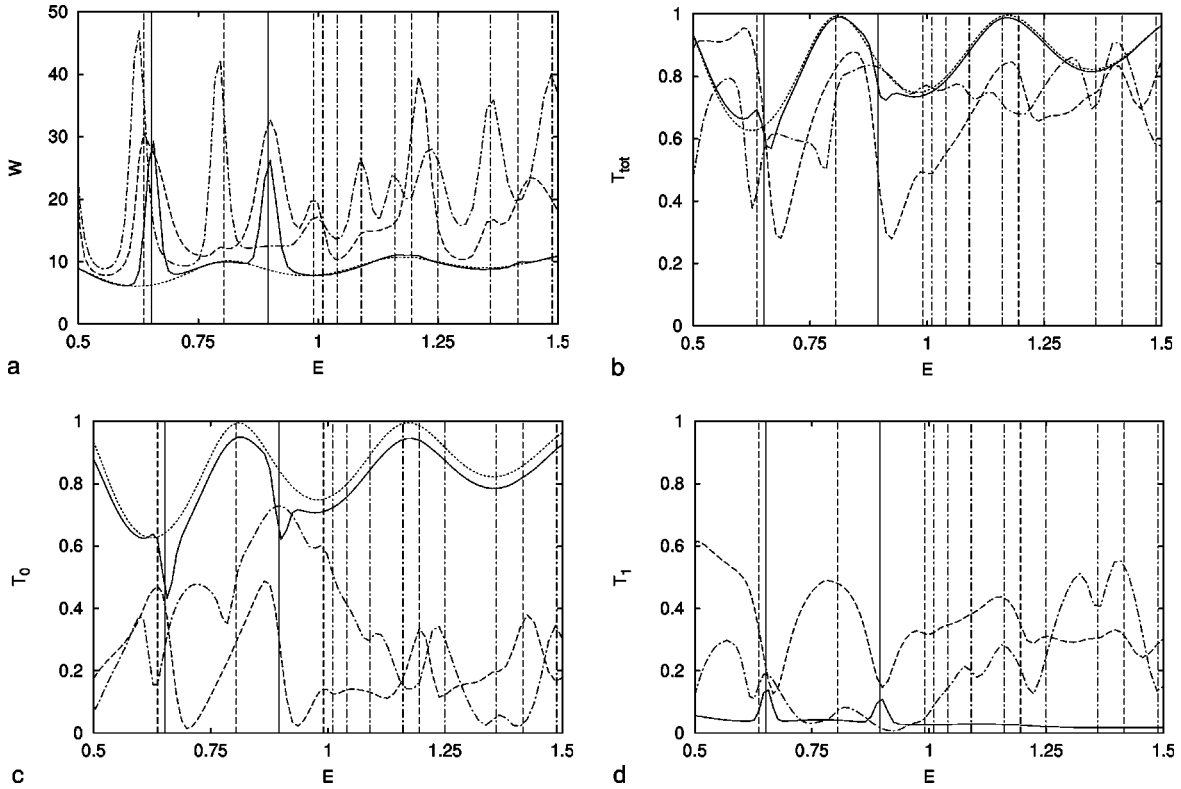


FIG. 17. Dwell time  $W$  [Eq. (27), panel (a)], total transmission  $T_{\text{tot}}$  (b), and transmissions  $T_0$  (c) and  $T_1$  (d) into the elastic and the first inelastic channel, respectively, as functions of the incoming energy  $E_{\text{in}}$  for a square well with oscillating bottom, Eq. (10), with  $V=2$ ,  $\gamma=0.9$ ,  $L=15$ ,  $\hbar=1$ ,  $m=0.5$ , and  $V_1=0$  (static case, dotted line)  $V_1=0.2$  (full), 1 (dashed), 2 (dot-dashed). Resonant energies  $E_{\text{in}}(\alpha, n_{\text{in}})$  are marked by vertical lines for  $n_{\text{in}}=1$  (full lines), 2 (dashed), and 3 (dot-dashed).

and outgoing energies

$$E_{\text{out}}(\alpha, n_{\text{out}}) = \epsilon_{\alpha} + n_{\text{out}} \hbar \omega, \quad (29)$$

so that  $m = n_{\text{out}} - n_{\text{in}}$  is the net number of photons gained or lost during the process. While these *multiphoton processes* appear inelastic from the point of view of static scattering, they do not violate quasienergy conservation and therefore are perfectly elastic in the Floquet picture. At the same time, the Floquet framework allows one to define multiphoton processes without any approximation. It is indispensable, in particular, in the regime between the adiabatic and the diabatic limit where the concept of an effective static potential does not apply. We emphasize that the concept of multiphoton processes is by no means new, but has been introduced as early as the 1960s, in the context of laser-atom interactions at high laser intensities (for a review, see, e.g., Ref. [48,49]).

We found evidence for this picture in the data obtained for all three models studied, in the transmission and reflection spectra as well as in the dwell time (27). Figure 17(a) shows the dwell time for the vertically oscillating well (10) as a function of  $E_{\text{in}}$  for various values of the driving amplitude, compared to the static case. The vertical lines mark resonances according to Eq. (28), for  $n_{\text{in}}=1, 2, 3$ . They enable us to interpret almost all of the visible peaks in terms of multiphoton processes. A global check of this interpretation is given in Fig. 18. All the identifiable resonances (dots in the  $\omega$ - $E$  plane) are located on lines given by Eq. (28) for

specific values of  $n_{\text{in}}$ . We have found resonances for a total number  $n_{\text{in}} + n_{\text{out}}$  of exchanged photons, up to six.

In a perturbative treatment of the driving, a multiphoton process with a net exchange of  $l$  photons with the field, would correspond to an  $|l|$ th-order term. One therefore expects a nonlinear dependence of the resonance strengths on

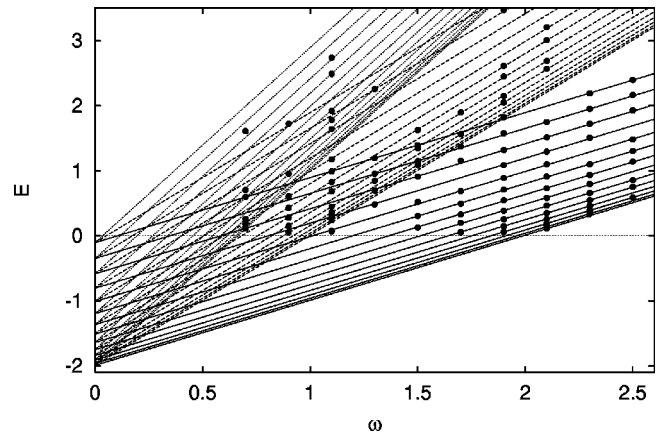


FIG. 18. Resonance positions in the  $\omega$ - $E$  plane (dimensionless units, full circles) for a square well with oscillating bottom [Eq. (10),  $V=2$ ,  $\gamma=0.9$ ,  $L=15$ ,  $\hbar=1$ , mass  $m=0.5$ ]. The bundles of parallel lines indicate resonant energies  $E = \epsilon_{\alpha} + n_{\text{in}} \hbar \omega$ , with  $n_{\text{in}} = 1, 2, 3$  (from below), related to bound-state energies  $\epsilon_{\alpha}$  in the static well.

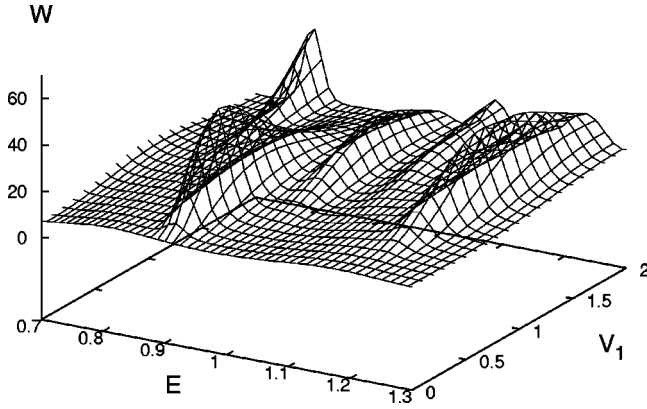


FIG. 19. Dwell time  $W$  as a function of incoming energy  $E_{\text{in}}$  and amplitude  $V_1$ , for a square well with oscillating bottom, Eq. (10), with  $V=3$ ,  $L=5$ ,  $\omega=1=\hbar$ , and  $m=0.5$ .

the driving amplitude. This is evidenced in Fig. 19. The dwell-time peak heights depend in a highly nonlinear and nonmonotonic manner on the oscillating part  $V_1$  of the potential.

Signatures of resonances are also visible in the transmission and reflection spectra. Data for the total transmission are presented in Fig. 17(b) in a similar way as for the dwell time in Fig. 17(a). The transmissions for sufficiently strong driving show a complicated energy dependence, totally different from the static case. The identification of individual reso-

nances and their association with multiphoton processes, however, is difficult. The reasons are complicated line shapes arising from interference of resonances with each other or with the background.

Our numerical method allowed us to calculate transmissions and reflections separately for the individual Floquet channels. Figure 17(c) is analogous to the previously discussed one, but refers to the “elastic” ( $n_{\text{in}}=0$ ) channel only. It shows similar structures as the total transmission, but a general reduction of the scattering into this channel with increasing amplitude of the driving. The corresponding increase of the flow into the other channels is demonstrated in Fig. 17(d) showing the case  $n_{\text{in}}=1$ .

All the data depicted up to now have been obtained for the square well with vertically oscillating bottom. Since the interpretation in terms of multiphoton processes is quantum mechanical and does not refer to the classical dynamics, qualitative differences to the results for the two other models are not expected. Figure 20 shows data for the smooth well with oscillating bottom, Eq. (12), for a selection of the quantities discussed above for the square well. The fact that one system supports pseudointegrable, the other chaotic classical dynamics, has no systematic consequences for the scattering in this regime.

The third model, the laterally oscillating square well, Eq. (6), is different from the previous two cases in that here the time-averaged potential, Eq. (15), never coincides with any instantaneous one. As a consequence, the diabatic and the

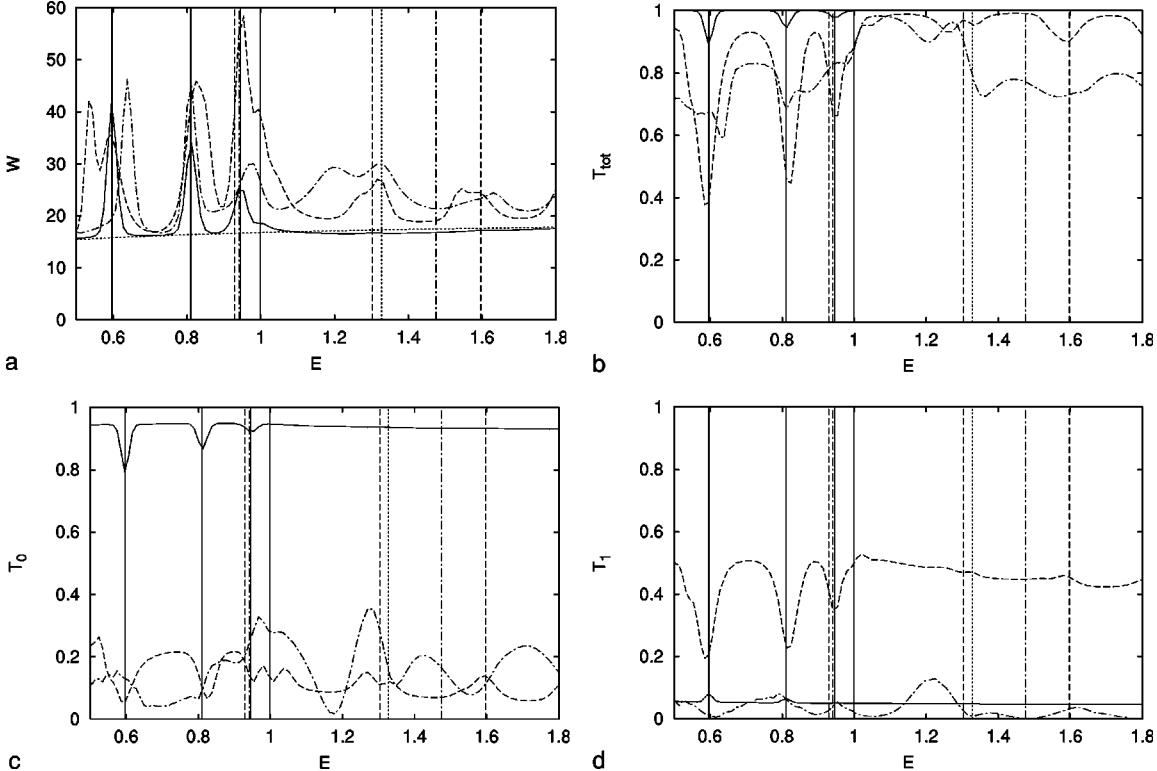


FIG. 20. Dwell time  $W$  (a), total transmission  $T_{\text{tot}}$  (b), transmissions  $T_0$  (c), and  $T_1$  (d) into the elastic and the first inelastic channel, respectively, as functions of the incoming energy  $E_{\text{in}}$  for a smooth well with oscillating bottom, Eq. (12), with  $V=2$ ,  $\gamma=0.9$ ,  $L=15$ ,  $\hbar=1$ ,  $m=0.5$ , and  $V_1=0.3$  (full line), 1.5 (dashed), 3 (dot-dashed). Resonant energies  $E_{\text{in}}(\alpha, n_{\text{in}})$  are marked by vertical lines for  $n_{\text{in}}=1$  (full lines), 2 (dashed), 3 (dot-dashed), and 4 (dotted); dimensionless units used.

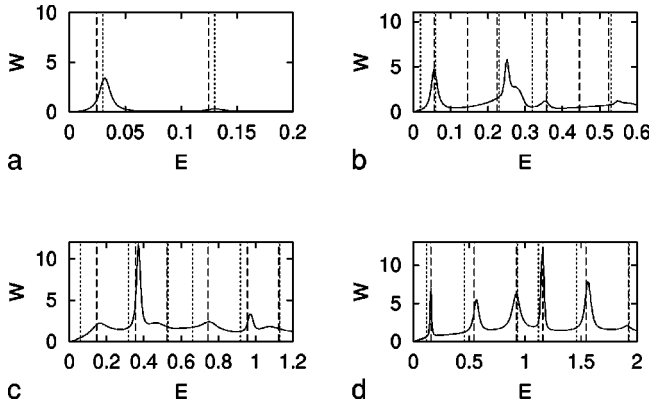


FIG. 21. Dwell time  $W$  as a function of the incoming energy  $E_{\text{in}}$ , for a laterally oscillating square well, Eq. (6), with dimensionless units,  $V = -1$ ,  $L = 2.5$ ,  $\lambda = 1$ ,  $m = 1 = \hbar$ , and  $\omega = 0.1$  (a), 0.3 (b), 0.6 (c), 1 (d). Resonant energies  $E_{\text{in}}(\alpha, n_{\text{in}})$  for the adiabatic and the diabatic limits are marked by dotted and dashed vertical lines, respectively.

adiabatic limits correspond to different potential shapes. This allows us to check the concept of multiphoton processes from a new perspective: In Fig. 21, the peaks in the dwell time are compared to the positions of resonances at eigenstates of the effective potential in the adiabatic and the diabatic limit for a number of driving frequencies spanning the transition from one limit to the other. The corresponding shift of the peak positions is clearly visible.

A more surprising consequence of the diabatic effective potential shape is discussed in the following section.

#### D. Tunneling at strong diabatic driving

As discussed in Sec. III C above, adiabatic and diabatic limits of the driving can be defined as  $\omega \gg t_{\text{pas}}^{-1}$  and  $\omega \ll t_{\text{pas}}^{-1}$ , respectively, where  $t_{\text{pas}}$  is the classical time for one round trip through the well at an energy just below its edge. In these limits, scattering occurs approximately at an effective static potential. In the adiabatic case, it is the instantaneous state of the time-dependent potential. In the diabatic case, it is the potential averaged over a period of the driving,  $V_{\text{eff}}(x) = T^{-1} \int_0^T dt V(x, t)$ .

The shape of the diabatic potential does not coincide with any instantaneous one. The laterally oscillating square well, Eq. (6), may even develop a central barrier and thus assume the form of a double well, see Eq. (17) and Fig. 14.

In this limit, the eigenstates of the effective potential are good approximations to the Floquet states of the driven system. For a sufficiently deep double well, quantum mechanics predicts the formation of tunnel doublets below the top of the central barrier, with a splitting that depends exponentially on the area below the barrier. In the present case, these states are resonances, so a doublet structure in the spectrum and corresponding tunneling in the time domain will occur only if the full width of the resonances is smaller than their separation. We demonstrate in Fig. 22 that this is indeed possible: The spectrum of the effective potential (panel a) shows a relatively wide doublet that appears as a double minimum in the total transmission (b) and in  $T_0$  (c), and as a double

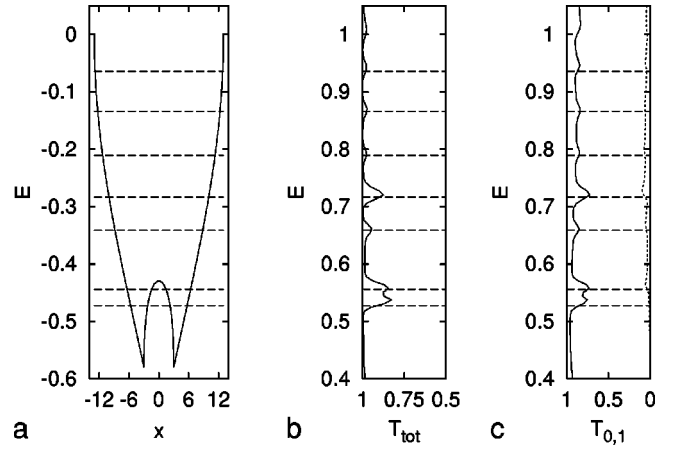


FIG. 22. (a) Effective potential (full line), (b) total transmission  $T_{\text{tot}}$  (full line, along abscissa) vs energy  $E_{\text{in}}$  (along ordinate), (c) partial transmissions  $T_0$  (full line) and  $T_1$  (dotted), for the laterally oscillating square well, Eq. (6), with  $\tilde{\lambda} > 1$ . In all three panels, the bound-state energies of the diabatic effective potential, corresponding to resonant energies  $E_{\text{in}}(\alpha, n_{\text{in}})$  (dimensionless units), are marked as horizontal dotted lines.

maximum in  $T_1$  (c). The different signature of the resonances in these quantities is readily understood, assuming that a long dwell time decorrelates the outgoing from the incoming conditions and thus drives transmissions as well as reflections towards intermediate values around 0.5.

In the time domain (Fig. 23), we observe exponentially decaying oscillations, with opposite phase, of the populations of the left and right half of the scattering region, giving clear evidence of a temporary tunneling of the scattering wave packet between the two wells. The observed period of the oscillation ( $T_{\text{obs}} \approx 42 \times 2\pi$ ) is in reasonable agreement with the value predicted on basis of the splitting  $\Delta E$  of the corresponding eigenstates of the effective potential ( $T_{\text{spl}} = 2\pi\hbar/\Delta E \approx 36 \times 2\pi$ ), taking into account the frequency reduction by the damping.

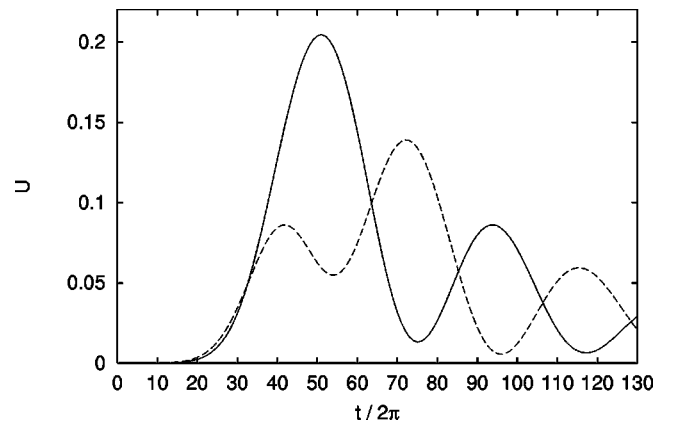


FIG. 23. Overlap of a scattering wave packet with the right (full line) and the left (dashed) half of the scattering region, vs time. The wave packet came in from the left with an energy near the center of the tunneling doublet visible in Fig. 22. The scattering potential and its parameters are as in Fig. 22.

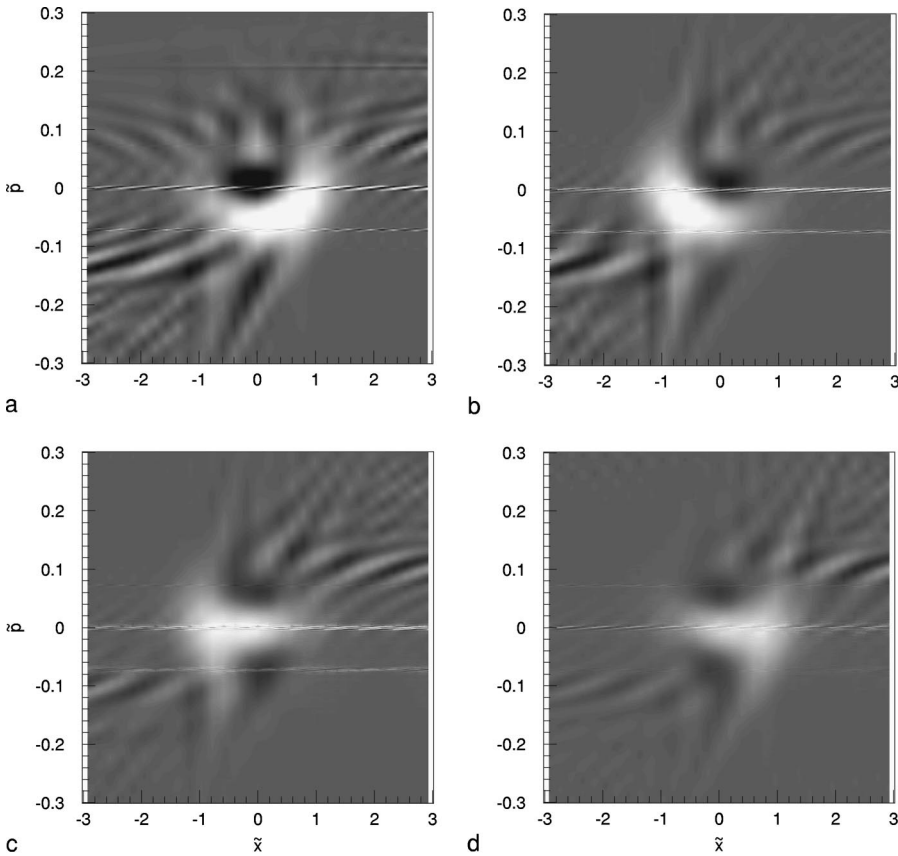


FIG. 24. Phase-space snapshots of the same tunneling wave packet as underlies Fig. 23, in terms of the Wigner function, at  $t/T=60$  (a), 70 (b), 80 (c), and 90 (d). The interval spanned corresponds roughly to a full tunneling cycle. The scattering potential and its parameters are as in Fig. 22.

A similar phenomenon has been studied in the context of strong laser irradiation of atomic hydrogen, likewise with a harmonic driving but with a Coulomb potential instead of a square well [50]. There, however, a high-frequency approximation was introduced that decouples the states within the well from the continuum. This precludes to study how this type of tunneling process manifests itself in scattering.

In the case of a laterally oscillating square *barrier*, a dual counterpart of the effect discussed above occurs [14]: The effective potential in the diabatic limit splits into a double barrier that accommodates quasibound Floquet states within its central well, giving rise to transport via tunneling at the energies of these metastable states.

Of course, the same interpretation in terms of tunneling through an effective central barrier must also apply to the model with explicit ac-driving term, Eq. (5). There, it is the inertia of the system that prevents its passing through the center of the well at high frequency and amplitude of the driving. In whatever “gauge,” the absence of energy conservation due to the driving implies that the concept of a static potential barrier is inadequate. In this sense, we are here dealing with “dynamical tunneling.”

At the same time, the observed phenomenon should clearly be distinguished from modifications of tunneling, including its coherent suppression, due to a periodic driving [51]. There, the *static* potential already possesses a double minimum giving rise to tunneling, which can then be further modified by the driving. Here, in contrast, it is only the driving that generates, in the first place, a central barrier in an otherwise purely attractive potential. To see the additional

effects reported in Ref. [51] would require to superpose a second driving with a suitable frequency, much slower than the diabatic one that produces the effective double-well potential shape.

### E. Quantum scattering in phase space

Although we remain marginally close to the classical limit in our numerical experiments, we still expect to see first indications of the intricate structures of the classical phase space, shown in the previous sections, in the quantum scattering. While our data are not suitable to identify the fingerprints of chaotic scattering in the spectral statistics of the  $S$  matrix [52], we are able to compare wave packets within the scattering region with the corresponding classical phase-space structure.

Details of the definition of the Wigner function in a discrete phase space, as it is underlying all our numerical calculations on the quantum level, are presented in Appendix E.

The same process as in Fig. 23 is shown in Figs. 24(a–d) in terms of snapshots of the Wigner function at four equidistant times, separated roughly by a quarter tunneling cycle. An unexpected feature clearly visible in this sequence is the return of the tunneling wave packet near zero momentum, thus forming a cyclic motion in phase space. This finding is consistent with a general analysis of tunneling in terms of the Wigner function [53]: The fraction of the Wigner function that tunnels moves along classical trajectories higher in energy than, i.e., *outside*, the separatrix emanating from the top of the tunneling barrier.

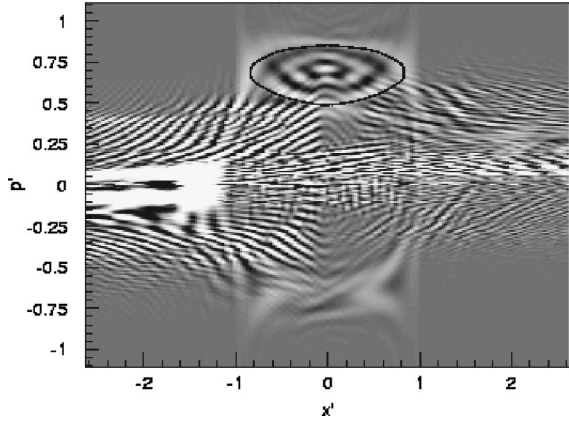


FIG. 25. Gray-scale plot (brightness increases with amplitude) of the Wigner function averaged over a few periods of the stroboscopic time evolution during scattering. Classical parameters are as in Fig. 11, and  $\hbar_{\text{eff}} = \hbar / (L^2 m \omega) = 1/49$  (a dimensionless effective quantum of action). The closed bold curve is the classical separatrix shown in Fig. 11.

A representative example of classical-quantum correspondence in terms of the Wigner function is shown in Fig. 25. We have chosen parameter values where the classical dynamics (cf. Fig. 11) is characterized by the coexistence of a global chaotic scattering area with a large regular island, inaccessible from the asymptotic regions, embedded in it. In the figure, the corresponding quantum phase space is represented in terms of the Wigner function for the wave packet, averaged over a few time steps while it is mainly located within the scattering region.

In the gray-scale presentation chosen, the incoming and the directly reflected components of the wave packet stand out as exceedingly bright regions, to the left of the scattering region, at positive and negative momentum. The interaction region itself can be discerned due to a population density generally higher inside than outside. Superposed, one distinguishes small-scale ripples, which give evidence of the coherence of the Wigner function and prove strongly parameter dependent, from oscillations of larger wavelength inside the scattering region. A comparison with the classical phase-space portrait, Fig. 11, suggests that these oscillations are signatures of the classical tori limiting the chaotic area from below, and of the regular island inside it. This is confirmed by our repeating, as a bold closed line, the outline of the island in the Wigner-function plot.

Given that this island is inaccessible for classical scattering trajectories, it surprises that it nevertheless shows up in the phase-space representation of a quantum scattering wave packet. Evidently, it can only be accessed by tunneling across the mixed boundary region separating the island from the chaotic sea. Indeed, we are here not yet far inside the semiclassical regime where such tunnel processes would be exponentially suppressed. A similar case of a classical regular island influencing the quantum scattering has been reported in Ref. [13].

## V. CONCLUSION

With this work, we have pursued a twofold intention: to provide particularly *simple* models that qualify as prototypes

of classical and quantum irregular models, and to come as close as possible to *realistic* experimental situations, specifically in mesoscopic physics. The key ingredient, in both regards, is a harmonic driving. It allows to reduce the number of spatial dimensions to one, and at the same time, captures the essence of most of the driving mechanisms available in the laboratory.

We have aimed at a comprehensive treatment of time-dependent scattering in the regime of large amplitude of the driving. In this respect, the Floquet approach used represents both an efficient tool for numerical calculations of the scattering matrix, transmission amplitudes, and dwell times, as well as a suitable framework to understand multiphoton processes at strong driving. Correspondingly, we used stroboscopic phase-space plots, deflection functions and dwell-time distributions as tools to visualize and classify the classical scattering dynamics.

We have shown that ac-driven one-dimensional scattering systems cover a wide spectrum of nonlinear classical dynamics, with properties ranging from pseudointegrable behavior via mixed phase-space characteristics up to strong chaos. We have identified features of the classical phase-space structures in Wigner representations of propagating wave packets. In this respect, a more quantitative analysis of quantum-classical correspondence in time-periodic scattering is desirable. It requires further quantum calculations in the truly semiclassical regime [16].

On the quantum-mechanical side, we have pointed out the role of multiphoton processes for the transmission. A strong driving can alter the features of the static scattering potential completely. This has become particularly evident when considering a *single* quantum well that, upon harmonic driving, behaves like an effective *double* well, with features of a diatomic molecule.

As mentioned in the Introduction, mesoscopic electronic devices represent promising experimental tools for studying driven quantum scattering and for observing the classical and quantum effects discussed throughout this work. High-mobility semiconductor microstructures have already proven ideal laboratories to investigate quantum-chaotic aspects of dc transport [54,55]. Quantum charge transport through such microstructures, which can be devised as electron billiards, exhibits clear signatures of the underlying classical dynamics determined by the confinement geometry. For instance, classical dwell-time distributions directly influence correlations in observed quantum conductance fluctuations [54].

An experimental extension to the time-dependent domain would enlarge the number of control parameters and allow for addressing the rich variety of complex-scattering phenomena an ac driving provides. Interesting effects are particularly expected for strong driving with a period comparable to the time of flight of an electron through the scattering region. This regime can nowadays be reached in ballistic mesoscopic transport: The typical time of flight through a micron-sized GaAs quantum well with electron density  $n_s \approx 5 \times 10^{15} \text{ m}^{-2}$  is of the order of  $10^{-11} \text{ s}$ . This corresponds to (radio)frequencies  $\omega$  in the range of some 100 GHz that have been employed in recent transport measurements [4].

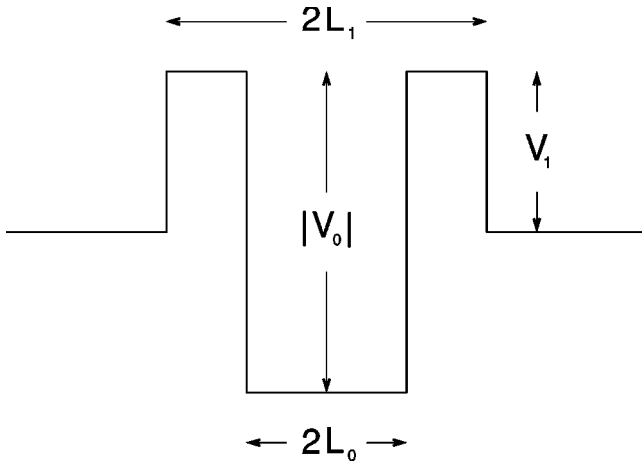


FIG. 26. Model of a quantum well with tunnel barriers.

Mesoscopic transport experiments often involve quantum wells or quantum dots weakly coupled to leads or reservoirs via tunneling barriers. A simplified one-dimensional model is sketched in Fig. 26. The conductance of such a device usually depends sensitively on the (Fermi) energy and on additional gate voltages that may change the depth or effective width of the quantum well. Charge transport is strongly affected and mediated by resonant states inside the well. To give an idea how an ac driving can alter the quantum transmission through such a device, we have computed the transmission and dwell times quantum mechanically for the model potential in Fig. 26. The potential with rectangular tunnel barriers is obtained by superimposing a barrier of width  $2L_1$  with a well of smaller width  $2L_0$ ,

$$V(x) = V_0 \theta(L_0 - |x|) + V_1 \theta(L_1 - |x|). \quad (30)$$

After the Kramers-Henneberger transformation the time-periodic driving leads to a laterally oscillating potential  $V(x - \lambda \cos(\omega t))$ . A similar double-barrier potential (without a well between the barriers) has been studied in Ref. [56] using the transfer-matrix approach for piecewise constant potentials [57].

The effect of the ac driving on the total transmission and the effective dwell time, Eq. (27), is depicted in Fig. 27. The different curves in both panels show the evolution of transmission and dwell time as a function of the incoming energy for increasing driving strength up to intermediate values of  $\lambda$ . For  $\lambda = 0$ , there is a maximum in the transmission and in the effective dwell time at  $E \approx 0.4$ , owing to resonant tunneling through the static double barrier. For finite driving this maximum is suppressed. Instead, distinct structures arise that are particularly clearly visible in the dwell time. They result from photonic coupling to quasibound states formed in the time-varying scattering potential (at energies  $\hbar\omega$  below the energy of the dwell time peaks). Thereby, the total transmission can be changed considerably, turning for instance the transmission maximum at  $E \approx 0.85$  into a sharp dip in the presence of an ac field. This shows that it is possible to use an ac driving for the control of transmission through quantum wells.

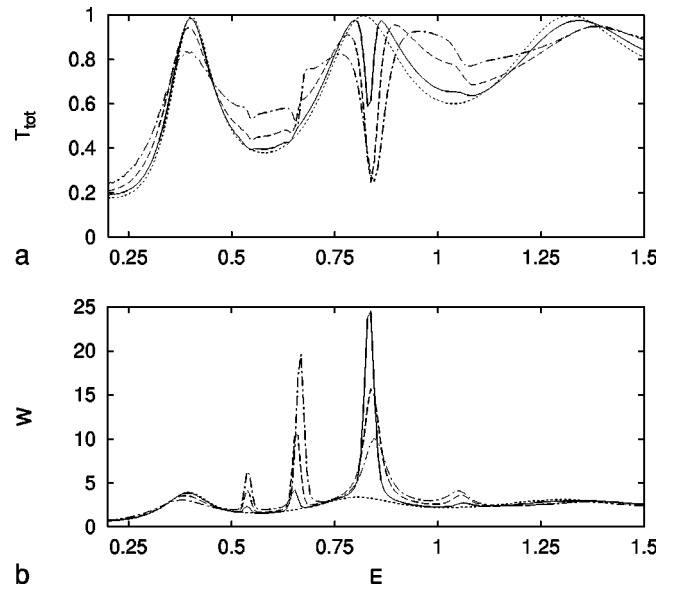


FIG. 27. Total transmission  $T_{\text{tot}}$  (upper panel) and dwell time  $W$  (lower panel) as functions of the incoming energy  $E$  for the laterally oscillating double-barrier well, Fig. 26 and Eq. (30), with  $V_0 = -1$ ,  $L_0 = 5$ ,  $V_1 = 0.5$ ,  $L_1 = 6$ ,  $\omega = 1$ ,  $m = 1 = \hbar$ , and different (lateral) driving amplitude  $\lambda = 0$  (static case, dotted line),  $\lambda = 0.25$  (full line),  $\lambda = 0.5$  (dashed line), and  $\lambda = 0.75$  (dashed-dotted line).

Effects arising at even stronger driving are shown in Fig. 28 for the dwell time. New groups of peaks appear at higher incoming energy (between  $E = 1.5$  and 2 and between  $E = 2.5$  and 3), which reflect coupling to resonant states in the oscillating well due to multiphoton processes at energies  $E_{\alpha, n_{\text{in}}}$  (28) with  $n_{\text{in}} = 2$  and 3. These peaks show up for a driving strength  $\lambda \geq 1$ .

The models for scattering systems treated here rely on a single-particle picture. A more realistic description of ac transport in mesoscopic devices, however, has to account for electron-electron interaction effects. They are particularly important if one deals with transport through quantum dots instead of vertical transport through quantum wells with con-

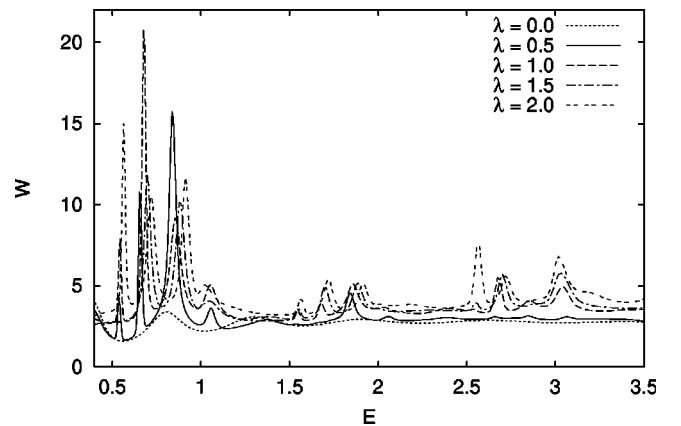


FIG. 28. Dwell time  $W$  as a function of the incoming energy  $E$  (dimensionless units) for the laterally oscillating double barrier well, Fig. 26, for the same parameters as in Fig. 27 but with different driving strength  $\lambda = 0, 0.5, 1, 1.5$ , and 2.

finement only in one spatial direction. Still, even for a perturbative time-periodic driving our knowledge of the role of interactions for the conductance is rather incomplete. Moreover, interaction effects on transport in the regime of strong driving remain an open field and their adequate treatment a challenge. Again, the Floquet approach may provide a convenient framework to account for the time periodicity, and interesting physics is expected from the interplay between interactions and strong time-periodic driving.

### ACKNOWLEDGMENTS

We have benefited from discussions with Christof Jung, Bruno Mirbach, Petr Šeba, and Mathias Wagner. We particularly thank Peter Hänggi for a thorough and critical reading of the manuscript, which helped to improve it a lot, and for various helpful discussions during the course of the work. One of us (TD) would like to thank for the warm hospitality enjoyed during stays (DFG Grant No. Di 511/4-1) in the group of Oriol Bohigas, Institut de Physique Nucléaire, Orsay, in the group of Thomas Seligman at the Centro de Ciencias Físicas, Cuernavaca, and, generously financed by the Max Planck Society, at the Max-Planck-Institut für Physik komplexer Systeme, Dresden, where parts of this work have been performed.

### APPENDIX A: CLASSICAL AND QUANTUM KRAMERS-HENNEBERGER TRANSFORMATIONS

#### 1. Classical transformations

Consider a charged particle in one dimension, subject to the total potential

$$V_{\text{tot}}(x, t) = V(x, t) + xg(t) \quad (\text{A1})$$

(the generalization to higher dimensions is straightforward). The scattering potential  $V(x, t)$  allows for the definition of asymptotically free states, but may be arbitrarily time dependent. The driving  $g(t)$  is also completely arbitrary here, in particular, it need not be periodic. In the representation in terms of a scalar potential or the *length gauge*, the Hamiltonian and the Lagrangian read, respectively,

$$H_1(x_1, p_1, t) = \frac{p_1^2}{2m} + V(x_1, t) + x_1g(t), \quad (\text{A2})$$

and

$$L_1(x_1, \dot{x}_1, t) = \frac{m}{2} \dot{x}_1^2 - V(x_1, t) - x_1g(t). \quad (\text{A3})$$

They lead to the equation of motion

$$\ddot{x}_1 = -\frac{1}{m}(V'(x_1, t) + g(t)), \quad (\text{A4})$$

with  $V'(x, t) = \partial V(x, t)/\partial x$ .

The driving term can be moved from the potential to the kinetic energy, by a gauge transformation with the generating function

$$F_m(x_m, t) = x_m p_g(t) \quad (\text{A5})$$

introducing

$$p_g(t) = m\dot{x}_g(t) = \int_{t_0}^t dt' g(t'), \quad x_g(t) = \frac{1}{m} \int_{t_0}^t dt' p_g(t'). \quad (\text{A6})$$

This defines the *momentum gauge*, where

$$\begin{aligned} L_m(x_m, \dot{x}_m, t) &= L_1(x_m, \dot{x}_m, t) + \frac{d}{dt} F_m(x_m, t) \\ &= \frac{m}{2} \dot{x}_m^2 + m\dot{x}_m \dot{x}_g(t) - V(x_m, t). \end{aligned} \quad (\text{A7})$$

From the momentum

$$p_m = m(\dot{x}_m + \dot{x}_g(t)), \quad (\text{A8})$$

canonically conjugate to  $x_m$ , one obtains the Hamiltonian

$$H_m(x_m, p_m, t) = \frac{1}{2m} [p_m - p_g(t)]^2 + V(x_m, t), \quad (\text{A9})$$

where the driving now appears as a magnetic-field term in the kinetic energy. The equations of motion generated by the Lagrangian (A7) and the Hamiltonian (A9), respectively, are identical to Eq. (A4).

The *acceleration gauge* is reached by a transformation generated by

$$F_a(x, t) = xp_g(t) + \frac{1}{2m} \int_{t_0}^t dt' (p_g(t'))^2, \quad (\text{A10})$$

instead of Eq. (A5). It leads to the Lagrangian

$$L'_a(x, \dot{x}, t) = \frac{m}{2} [\dot{x} + \dot{x}_g(t)]^2 - V(x, t). \quad (\text{A11})$$

By an additional point transformation

$$x_a = x + x_g(t), \quad (\text{A12})$$

it takes the form

$$L_a(x_a, \dot{x}_a, t) = \frac{m}{2} \dot{x}_a^2 - V(x_a - x_g(t), t) \quad (\text{A13})$$

which implies that

$$p_a = m\dot{x}_a \quad (\text{A14})$$

is the corresponding momentum canonically conjugate to  $x_a$ . The transformed Hamiltonian thus reads

$$H_a(x_a, p_a, t) = \frac{1}{2m} p_a^2 + V(x_a - x_g(t), t). \quad (\text{A15})$$

The equation of motion in the present frame is now lacking an additive driving term,

$$\ddot{x}_a = -\frac{1}{m} V'(x_a - x_g(t), t). \quad (\text{A16})$$

Equation (6) is retained by setting  $V(x, t) = V_0 f(x)$  and  $g(t) = -qE \sin(\omega t)$ .

## 2. Quantum transformation

Starting from the Hamiltonian (A2), the Schrödinger equation in the length gauge reads

$$i\hbar \frac{\partial}{\partial t} \psi_1(x, t) = \left[ -\frac{\hbar^2}{2m} \frac{\partial^2}{\partial x^2} + V(x, t) + xg(t) \right] \psi_1(x, t). \quad (\text{A17})$$

By a shift in momentum, cf. Eq. (A8),

$$\psi_1(x, t) = \exp\left[-\frac{i}{\hbar} x p_g(t)\right] \psi_m(x, t), \quad (\text{A18})$$

one arrives at the Schrödinger equation in the momentum gauge,

$$i\hbar \frac{\partial}{\partial t} \psi_m(x, t) = \left[ \frac{1}{2m} \left\{ \frac{\hbar}{i} \frac{\partial}{\partial x} - p_g(t) \right\}^2 + V(x, t) \right] \psi_m(x, t), \quad (\text{A19})$$

consistent with the classical Hamiltonian (A9) in this gauge.

The quantum transformation leading from here to the acceleration gauge,

$$\begin{aligned} \psi_m(x, t) = \exp \left[ -\frac{i}{\hbar} \left\{ \frac{1}{2m} \int_{t_0}^t dt' (p_g(t'))^2 \right. \right. \\ \left. \left. - x_g(t) \frac{\hbar}{i} \frac{\partial}{\partial x} \right\} \right] \psi_a(x, t) \end{aligned} \quad (\text{A20})$$

comprises both a change in phase corresponding to the second term in the generating function (A10), and a coordinate shift, cf. Eq. (A12). The transformed wave function  $\psi_a(x, t)$ , after replacing  $x \rightarrow x_a - x_g(t)$ , solves the Schrödinger equation

$$\begin{aligned} i\hbar \frac{\partial}{\partial t} \psi_a(x_a, t) = \left[ \frac{1}{2m} \left\{ \frac{\hbar}{i} \frac{\partial}{\partial x_a} - p_g(t) \right\}^2 \right. \\ \left. + V(x_a - x_g(t), t) \right] \psi_a(x_a, t), \end{aligned} \quad (\text{A21})$$

in accordance with the classical Hamiltonian (A15).

## APPENDIX B: POWER-LAW DECAY OF THE DWELL-TIME DISTRIBUTION FOR THE VERTICALLY OSCILLATING SQUARE WELL

The resonance condition for trajectories in the vertically oscillating square well that need  $l$  periods of the driving to cross the well, reads [cf. Eq. (10)]

$$\tilde{p}_l = \frac{1}{l\pi}, \quad l = 1, 2, \dots \quad (\text{B1})$$

see Fig. 1 in Sec. III A.

Whether a trajectory is trapped in the well depends further on its kinetic energy  $\tilde{T} = \tilde{p}^2/2$ . If  $\tilde{V}_0 - \tilde{V}_1 + \tilde{T} > 0$ , it can leave even at a minimum of the driving. If, on the other hand,  $\tilde{V}_0 + \tilde{V}_1 + \tilde{T} < 0$ , it cannot even escape at a maximum. Only in the intermediate regime  $-\tilde{V}_0 - \tilde{V}_1 < \tilde{T} < -\tilde{V}_0 + \tilde{V}_1$ , *open* and *closed windows* alternate in time, during which trajectories with kinetic energy  $\tilde{T}$  can leave or not. Their respective durations are

$$\tilde{t}_{\text{closed}} = \gamma \tilde{P}, \quad \tilde{t}_{\text{open}} = (1 - \gamma) \tilde{P}, \quad (\text{B2})$$

where  $\tilde{P} = 2\pi$  is the dimensionless period of the driving, and the relative measure of the trapped initial conditions is

$$\gamma = 1 - \frac{1}{\pi} \arccos \frac{2|\tilde{V}_0| - \tilde{p}^2}{2\tilde{V}_1}. \quad (\text{B3})$$

The condition that there exist both open and closed windows implies a lower bound on the resonant momenta,  $\tilde{p}_l^2/2 - |\tilde{V}_0| + \tilde{V}_1 \geq 0$ . Since the resonant momenta decrease with order  $l$ , this amounts to an upper bound on  $l$ ,

$$l \leq l_{\text{max}} = \text{int} \left( \frac{1}{\pi \sqrt{2(|\tilde{V}_0| - \tilde{V}_1)}} \right). \quad (\text{B4})$$

Equation (B4) shows that in order to create a large number of resonances,  $l_{\text{max}} \gg 1$ ,  $|\tilde{V}_0| - \tilde{V}_1$  should be small, that is, the maximum of the oscillating potential should almost reach the edges of the static well.

If trajectories with momentum  $\tilde{p}_l$  inside the well have entered during an open window, they will leave immediately once they reach the other side of the well (Fig. 3). For a scattering trajectory, in order to remain trapped for a longer time, a small deviation from the resonance condition is needed,

$$\tilde{p}_{l,\varepsilon} = (1 + \varepsilon) \tilde{p}_l, \quad (\text{B5})$$

where  $\varepsilon$  can have either sign, but must at least be so small that the corresponding interval around  $\tilde{p}_l$  does not overlap with the adjacent  $\varepsilon$  neighborhoods of  $\tilde{p}_{l \pm 1}$ . This means  $\varepsilon < 1/l$ .

Even for  $\tilde{p}_{l,\varepsilon}$ , in particular if  $\varepsilon \ll 1$ , only a small fraction of incoming trajectories will remain temporarily trapped (Fig. 29). The sought dwell-time distribution therefore depends on two factors, the probability  $P_{\text{ls}}(\varepsilon)$  to take the long sojourn and the distribution  $P(\tilde{t}|\text{ls})$  of dwell times for the long sojourns, given the distribution of  $\varepsilon$ . They will be discussed in this order.

In order to head for a long sojourn, a trajectory that entered within an open window must be in a closed window once it hits the opposite side of the well for the first time,

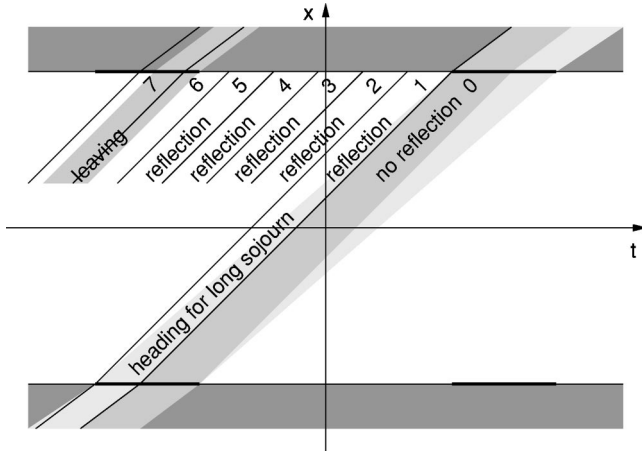


FIG. 29. Schematic space-time representation of a bundle of almost trapped trajectories, with near resonant momentum  $\tilde{p}_{1,\epsilon}$ , see Eq. (B5). While all of the incoming trajectories with resonant momentum  $\tilde{p}_1$  (light gray band) leave at the next open window (bold sections of the horizontal lines) of the potential, part of those with  $\tilde{p}_{1,\epsilon}$  (right darker band) head for a long sojourn. They leave (left darker band) only after, in this case, six or seven reflections at the potential steps, respectively, represented stroboscopically within the same period of the driving.

which in turn defines a time interval for the initial conditions, see Fig. 29. Its duration coincides with the advance or delay, after crossing the well once, of trajectories with  $\tilde{p}_{1,\epsilon}$  with respect to the resonant trajectories with  $\tilde{p}_1$ ,

$$\tilde{t}_{1,\epsilon} = \frac{2\tilde{L}}{\tilde{p}_1} - \frac{2\tilde{L}}{\tilde{p}_{1,\epsilon}} = \frac{2\pi l\epsilon}{1+\epsilon}. \quad (\text{B6})$$

The relative measure of these initial conditions is thus

$$P_{\text{ls}}(\epsilon) = \frac{\tilde{t}_{1,\epsilon}}{\tilde{T}} = \frac{l\epsilon}{1+\epsilon}. \quad (\text{B7})$$

It cannot exceed unity since  $\epsilon < 1/l$ .

In a stroboscopic representation, the narrow bundle of trajectories on a long sojourn is advanced (delayed) with respect to the “trailing (leading) edge” of the closed window, by  $\tilde{t}_{1,\epsilon}$  per passage across the well (Fig. 29). The minimum number of reflections necessary to reach the leading (trailing) edge of the preceding (subsequent) open window and to leave the well therefore is

$$n'_{l,\epsilon} = \text{int}\left(\frac{\tilde{t}_{\text{closed}}}{\tilde{t}_{1,\epsilon}}\right) = \text{int}\left(\frac{\gamma(1+\epsilon)}{l\epsilon}\right). \quad (\text{B8})$$

This occurs for a fraction

$$\begin{aligned} P(n'_{l,\epsilon}) &= 1 - \left[ \frac{\gamma(1+\epsilon)}{l\epsilon} - \text{int}\left(\frac{\gamma(1+\epsilon)}{l\epsilon}\right) \right] \\ &= 1 - \left( \frac{\gamma(1+\epsilon)}{l\epsilon} \right) \bmod 1 \end{aligned} \quad (\text{B9})$$

of the trajectories in the bundle. The remaining trajectories, with weight  $1 - P(n_{l,\epsilon})$ , leave at the “next exit,” i.e., after  $n''_{l,\epsilon} = n'_{l,\epsilon} + 1$  reflections.

It thus turns out that the number of reflections, and with it the dwell time, is deterministically related to  $\epsilon$ —up to the choice between  $n'_{l,\epsilon}$  and  $n''_{l,\epsilon}$ . However, as only high values  $l \gg 1$  and  $\gamma \lesssim 1$  are of interest, we replace those two reflection numbers, with small relative error, by a single value, their weighted mean (not necessarily integer),

$$v_{l,\epsilon} = P(n'_{l,\epsilon})n'_{l,\epsilon} + P(n''_{l,\epsilon})n''_{l,\epsilon} = \frac{\gamma(1+\epsilon)}{l\epsilon}, \quad (\text{B10})$$

to obtain the dwell time

$$\tilde{t}_{l,\epsilon} = v_{l,\epsilon} \frac{2\tilde{L}}{\tilde{p}_{1,\epsilon}} = \frac{2\pi\gamma}{\epsilon}. \quad (\text{B11})$$

Considering only narrow windows  $\epsilon \ll 1$  around each  $\tilde{p}_l$ , we can assume the momentum inside the well to be approximately equidistributed if the distribution of the incoming momentum is smooth on a scale  $\tilde{p}_l - \tilde{p}_{l+1}$ . Equation (B5) then implies that also  $\epsilon$  is equidistributed, and we obtain the dwell-time distribution for long sojourns

$$P(\tilde{t}|\text{ls}) = \left| \frac{d\tilde{t}}{d\epsilon} \right|^{-1} P(\epsilon) \sim \frac{l}{2\pi\gamma\tilde{t}^2}. \quad (\text{B12})$$

By means of Eq. (B11),  $\epsilon$  is replaced by  $\tilde{t}$  also in Eq. (B7),

$$P_{\text{ls}}(\tilde{t}) \approx l\epsilon = \frac{2\pi\gamma}{\tilde{t}}, \quad (\text{B13})$$

so that finally, for the  $l$ th resonance,

$$P_l(\tilde{t}) = P(\tilde{t}|\text{ls})P_{\text{ls}}(\tilde{t}) \sim \frac{l}{\tilde{t}^3}. \quad (\text{B14})$$

Equation (B14) shows that higher resonances contribute stronger to the dwell-time distribution.

The unknown  $\tilde{t}$ -independent proportionality factor in Eq. (B14) depends on the distribution of  $\epsilon$  and with it, on that of the incoming momenta. Since the respective  $\epsilon$  neighborhoods around the  $\tilde{p}_l$  have been defined so as to be disjunct, their contributions to the total dwell-time distribution can be superposed independently,

$$P(\tilde{t}) = \sum_l P_l(\tilde{t}) \sim \tilde{t}^{-3}, \quad \tilde{t} \gg 1. \quad (\text{B15})$$

The same reasoning, with only minor modifications, applies also to the distribution of dwell times in “domino billiards,” i.e., zigzag chains of rectangular billiards [33]. A more general derivation of the  $\tilde{t}^{-3}$  decay of the dwell-time distribution is presented in Ref. [31].

### APPENDIX C: CLASSICAL MAP FOR SCATTERING AT A Laterally Oscillating Square Well or Barrier

We describe the scattering at the laterally oscillating square well (6) in terms of a map from one encounter with either one of the moving walls to the next. It is thus based on a Poincaré surface of section that depends on time (the two walls can be conceptually merged into one by taking the reflection symmetry of the system with respect to the center of the well into account). Accordingly, we denote by  $\tilde{x}_n$ ,  $\tilde{p}_n$ ,  $\tilde{t}_n$ , the position, momentum, and time, respectively, at the  $n$ th collision, scaled as in Eq. (8). In addition, we introduce the binary-valued auxiliary variable  $i_n$ . It takes the values 1 (0), if immediately after the collision, the trajectory continues inside (outside) the well. For completeness, we include the case of a moving square *barrier*.

The calculation of  $\tilde{x}_{n+1}$ ,  $\tilde{p}_{n+1}$ ,  $\tilde{t}_{n+1}$  and  $i_{n+1}$  is performed in three steps:

*Calculation of  $\tilde{t}_{n+1}$ .* We define

$$F^\pm(\tilde{x}_n, \tilde{p}_n, \tilde{t}_n; \tilde{t}) = \tilde{x}_n + \tilde{p}_n(\tilde{t} - \tilde{t}_n) + \tilde{x}^\pm(\tilde{t}), \quad (\text{C1})$$

where

$$\tilde{x}^\pm(\tilde{t}) = \pm 1 + \tilde{\lambda} \cos \tilde{t} \quad (\text{C2})$$

are the positions of the right and left wall, respectively, at time  $\tilde{t}$ . The zeros of  $F^\pm(\tilde{x}_n, \tilde{p}_n, \tilde{t}_n; \tilde{t})$  are the times when a freely moving particle, starting at time  $\tilde{t}_n$  and position  $\tilde{x}_n$  with momentum  $\tilde{p}_n$  crosses the right or the left wall of the well. Therefore, possible candidates for  $\tilde{t}_{n+1}$  are determined by

$$F^\pm(\tilde{x}_n, \tilde{p}_n, \tilde{t}_n; \tilde{t}_{n+1}^\pm) = 0, \quad (\text{C3})$$

so that

$$\tilde{t}_{n+1} = \min_{\tilde{t}_{n+1} > \tilde{t}_n} (\tilde{t}_{n+1}^+, \tilde{t}_{n+1}^-). \quad (\text{C4})$$

The zeros  $\tilde{t}_{n+1}^\pm$  have to be calculated numerically. If the inequality  $\tilde{t}_{n+1} > \tilde{t}_n$  cannot be fulfilled, no further collision with the walls of the well takes place and the trajectory continues freely to  $\tilde{x} \rightarrow \text{sgn}(\tilde{p}_n) \infty$  with momentum  $\tilde{p}_n$ .

*Calculation of  $\tilde{x}_{n+1}$ .* Once the time  $\tilde{t}_{n+1}$  of the  $n+1$ st collision is known, one has immediately,

$$\tilde{x}_{n+1} = \tilde{x}^\pm(\tilde{t}_{n+1}) \quad \text{if} \quad \tilde{t}_{n+1} = \tilde{t}_{n+1}^\pm. \quad (\text{C5})$$

*Calculation of  $\tilde{p}_{n+1}$  and  $i_{n+1}$ .* The fate of a trajectory encountering a moving potential step depends on whether it comes from the low or the high side of the step, and on its momentum relative to the step. The first condition is encoded in  $i_n$ . The second refers, specifically, to the kinetic energy  $T_1(\tilde{p}_1) = (\tilde{p}_1)^2/2$  in the reference frame moving with the well, i.e., in the length gauge defined in Appendix A, compared to

$\tilde{V}_0$ , the well depth (or barrier height if  $\tilde{V}_0 > 0$ ). In that reference frame, the momentum is  $\tilde{p}_{1n} = \tilde{p}_n - \tilde{p}_g(\tilde{t}_{n+1})$ , denoting  $\tilde{p}_g(\tilde{t}) = -\tilde{\lambda} \sin \tilde{t}$ , the velocity of the well in the acceleration gauge. By going into the length gauge and defining the auxiliary variable

$$\tilde{V}_n = |\tilde{V}_0| \left( \frac{3}{2} - \left| i_n - \text{sgn}(\tilde{V}_0) - \frac{1}{2} \right| \right), \quad (\text{C6})$$

the various cases reduce to two:

$T_1(\tilde{p}_{1n}) < \tilde{V}_n$ : reflection

$$i_{n+1} = i_n, \quad (\text{C7})$$

$$\tilde{p}_{1n+1} = -\tilde{p}_n. \quad (\text{C8})$$

$T_1(\tilde{p}_{1n}) > \tilde{V}_n$ : transmission

$$i_{n+1} = 1 - i_n, \quad (\text{C9})$$

$$\tilde{p}_{1n+1} = \text{sgn}(\tilde{p}_{1n}) \sqrt{\tilde{p}_{1n}^2 + 2(2i_n - 1)\tilde{V}_0}. \quad (\text{C10})$$

For a trajectory entering the interaction region from the left at phase  $\phi_0$  of the driving and with momentum  $\tilde{p} > 0$ , the initial conditions are  $\tilde{t}_0 = \phi_0$ ,  $\tilde{x}_0 = \tilde{x}^+(\tilde{t}_0)$ ,  $\tilde{p}_0 = \tilde{p}$ , and  $i_0 = 0$ .

### APPENDIX D: FOURIER EXPANSION OF THE Laterally Oscillating Square Well

The temporal Fourier series for the laterally oscillating square well potential is defined by

$$\begin{aligned} V(x, t) &= V \theta(L - |x - \lambda \cos(\omega t)|) \\ &= \frac{a_0(x)}{2} + \sum_{j=1}^{\infty} [a_j(x) \cos(\omega t) + b_j(x) \sin(\omega t)]. \end{aligned} \quad (\text{D1})$$

Due to time-reversal invariance,  $V(x, t) = V(x, -t)$ , the sine coefficients  $b_j(x)$  vanish and

$$a_j(x) = \frac{2}{T} \int_0^T dt V(x, t) \cos(j\omega t), \quad (\text{D2})$$

for all positive integers  $j$ . The time average of the potential is given by

$$\bar{V}(x) = \frac{a_0(x)}{2} = \frac{1}{T} \int_0^T dt V(x, t). \quad (\text{D3})$$

Introducing  $\tau = \omega t$  and using  $\theta(\alpha - |\beta|) = \theta(\beta + \alpha) - \theta(\beta - \alpha)$ , one has

$$a_j(x) = \frac{V}{\pi} (I_j^+ - I_j^-), \quad (\text{D4})$$

where

$$I_j^\pm = \int_0^{2\pi} d\tau \theta(x \pm L - \lambda \cos \tau) \cos j\tau = I_j^+(\pm L). \quad (\text{D5})$$

Hence it suffices to calculate  $I_j^+$ . The Heaviside function restricts the integration range in Eq. (D5) to  $x+L > \lambda \cos \tau$ . There are three cases:

$$I_j^+ = \begin{cases} 0, & x+L \leq -\lambda, \\ \int_{\tau_1}^{\tau_2} d\tau \cos j\tau, & -\lambda < x+L < \lambda, \\ \int_0^{2\pi} d\tau \cos j\tau = 2\pi \delta_j, & x+L \geq \lambda. \end{cases} \quad (\text{D6})$$

For the second option, the integration range is given by the solutions of  $x+L = \lambda \cos \tau$ , namely

$$\tau_1 = \arccos\left(\frac{x+L}{\lambda}\right), \quad \tau_2 = 2\pi - \tau_1. \quad (\text{D7})$$

Therefore in this case, using  $\arccos(x) = \pi - \arccos(-x)$ ,

$$I_0^+ = 2 \arccos\left(-\frac{x+L}{\lambda}\right), \quad I_j^+ = -\frac{2}{j} \sin\left[j \arccos\left(\frac{x+L}{\lambda}\right)\right], \quad (\text{D8})$$

where  $j \geq 1$ . All three cases can be summarized as

$$I_0^+ = 2\pi \theta(x+L-\lambda) - 2\theta(\lambda - |x+L|) \arccos\left(-\frac{x+L}{\lambda}\right), \quad (\text{D9})$$

$$I_j^+ = -\frac{2}{j} \theta(\lambda - |x+L|) \sin\left[j \arccos\left(\frac{x+L}{\lambda}\right)\right]. \quad (\text{D10})$$

With Eq. (D5), this implies in particular

$$I_0^+ - I_0^- = 2\pi \theta(L+\lambda - |x|) - 2 \sum_{+,-} \theta(\lambda - |L \pm x|) \times \arccos\left(\frac{L \pm x}{\lambda}\right). \quad (\text{D11})$$

Finally, with the help of Eqs. (D3) and (D4), the time-averaged potential is obtained as (see Fig. 14)

$$\bar{V}(x) = V\left(\theta(L+\lambda - |x|) - \frac{1}{\pi} \sum_{+,-} \theta(\lambda - |L \pm x|) \arccos\left(\frac{L \pm x}{\lambda}\right)\right). \quad (\text{D12})$$

After scaling according to Eq. (8), this is equivalent to Eqs. (16) and (17). Likewise, for  $j \geq 1$ ,

$$a_j(x) = -\frac{2V}{j\pi} \sum_{+,-} \theta(\lambda - |x \pm L|) \sin\left[j \arccos\left(\frac{x \pm L}{\lambda}\right)\right]. \quad (\text{D13})$$

As the potential, Fourier expanded in Eq. (D1), has finite discontinuities, one expects a slow algebraic decay of its Fourier coefficients. Indeed, according to Eq. (D13),

$$|a_j(x)| \sim \frac{1}{j}. \quad (\text{D14})$$

The same applies to the coefficients  $2c_{\pm|m|}(x) = a_{|m|}(x) \mp ib_{|m|}(x)$  of  $V(x,t) = \sum_{m=-\infty}^{\infty} c_m(x) e^{im\omega t}$ , i.e.,  $|c_m(x)| \sim 1/|m|$ . Since in the Hamiltonian (26), the kinetic energy is time independent, one concludes for its Fourier coefficients,

$$||H_m(x,p)|| \sim \frac{1}{|m|}, \quad m \neq 0. \quad (\text{D15})$$

#### APPENDIX E: DEFINITION OF THE WIGNER FUNCTION FOR DISCRETE CONFIGURATION AND MOMENTUM SPACE

The definition of quantum-mechanical phase-space representations depends on the topology of phase space. This is obvious for the Husimi distribution, through the dependence on phase-space topology of the coherent states on which it is based, but it is also true for the Wigner function. Consider first the case of action-angle variables  $p$  and  $\theta$ , where  $\theta$  is cyclic so that the phase space assumes the topology of a cylinder, implying discretization of  $p$ ,  $p_l = \hbar l$ . A naive application of the definition of the Wigner function for a plane phase space,

$$W(p, \theta) = \frac{1}{2\pi\hbar} \int_{-\infty}^{\infty} d\theta' e^{-ip\theta'/\hbar} \psi^*\left(\theta - \frac{\theta'}{2}\right) \psi\left(\theta + \frac{\theta'}{2}\right), \quad (\text{E1})$$

taking the periodicity of the wave function,  $\psi(\theta + 2\pi) = \psi(\theta)$ , into account, results in

$$W(p, \theta) = \sum_{l=-\infty}^{\infty} W_l(\theta) \delta\left(p - \frac{\hbar}{2} l\right), \quad (\text{E2})$$

$$W_l(\theta) = \sum_{l'=-\infty}^{\infty} \exp(2\pi i l' \theta) \tilde{\psi}_{(l-l')/2}^* \tilde{\psi}_{(l+l')/2}, \quad (\text{E3})$$

where  $\tilde{\psi}_l = (2\pi)^{-1/2} \int_0^{2\pi} d\theta \exp(-il\theta) \psi(\theta)$  is the action representation of  $\psi(\theta)$ .

This Wigner function has support also at unphysical, half-integer values of the action in units of  $\hbar$ . However, due to the parity

$$W_l(\theta + \pi) = \begin{cases} W_l(\theta), & l \text{ even,} \\ -W_l(\theta), & l \text{ odd,} \end{cases} \quad (\text{E4})$$

it exhibits alternating signs at alternating values of  $l$  in the region  $\pi \leq \theta < 2\pi$ . Any coarse graining of the action on the scale of  $\hbar$  will essentially remove all structure there, while all the relevant information is already contained in the other half of angle space.

The redundancy can be removed by an evaluation of the angle integral in Eq. (E1), more appropriate to the cylindrical phase space, restricting the integration to a single period of  $\theta$  [58]. The choice of the limits of integration is then determined by the requirement that the Wigner function be real valued. It leads to the modified definition

$$W(p, \theta) = \frac{1}{2\pi\hbar} \int_{-\pi}^{\pi} d\theta' e^{-ip\theta'/\hbar} \psi^* \left( \theta - \frac{\theta'}{2} \right) \psi \left( \theta + \frac{\theta'}{2} \right). \quad (\text{E5})$$

The Wigner function now has support only at physical values of  $p$ ,

$$W(p, \theta) = \sum_{l=-\infty}^{\infty} W_l(\theta) \delta(p - 2\pi\hbar l), \quad (\text{E6})$$

where

$$W_l(\theta) = \sum_{l'=-\infty}^{\infty} e^{il'\theta} R_{l,l'}, \quad (\text{E7})$$

$$R_{l,l'} = \begin{cases} \tilde{\psi}_{l-l'/2}^* \tilde{\psi}_{l+l'/2}, & l \text{ even,} \\ \frac{1}{\pi} \sum_{l''=-\infty}^{\infty} \frac{(-1)^{l''}}{l''+1/2} \tilde{\psi}_{l-l'/2-(l''+1/2)}^* \tilde{\psi}_{l+l'/2-(l''+1/2)}, & l \text{ odd.} \end{cases} \quad (\text{E8})$$

The removal of the spurious, half-integer values of the action and the rescaling of the relevant part of phase space have been achieved at the expense of an additional summation in the direction of the main diagonal of the  $(l, l')$  lattice.

Another situation frequently encountered in the quantum mechanics of classically chaotic systems requires to define Wigner functions on a torus: the quantization of maps of the square with periodic boundary conditions, for example, the baker [59,60] or the cat map [61]. Here, the periodicity of each variable entails the discretization of the eigenvalues of the other, canonically conjugate one. A second, more practical application is the numerical treatment of spatially extended systems, using alternately a box with equidistant, discrete positions in configuration space and plane waves with periodic boundary conditions in this box for representation. Independently of applications, discrete phase spaces may also be considered a laboratory of quantum dynamics in its own right [62].

Specifically, we require periodicity in position,  $\psi(x+L) = \psi(x)$  and in momentum,  $\tilde{\psi}(p+M) = \tilde{\psi}(p)$ . This implies, respectively, discretization of momentum  $p_l = 2\pi\hbar l/L$  and position  $x_m = 2\pi\hbar m/M$ . Assuming the entire phase space of size  $LM$  to accommodate  $N$  Planck cells, the quantization condition

$$LM = 2\pi N\hbar \quad (\text{E9})$$

restricts the quantum of action to the discrete values  $\hbar = LM/(2\pi N)$ . If we place the origin in the center of the  $(x, p)$  ‘‘unit cell,’’ we find as admissible values of position and momentum,  $p_l = lM/N$  and  $x_m = mL/N$ ,  $l, m = -N/2, \dots, N/2-1$ , respectively. The two corresponding bases  $\{|l\rangle\}$ ,  $\{|m\rangle\}$  then obey the relations

$$\langle l|m\rangle = \frac{1}{\sqrt{N}} \exp\left(-2\pi i \frac{lm}{N}\right), \quad (\text{E10})$$

$$\langle l'|l\rangle = \delta_{(l'-l) \bmod N} \quad \langle m'|m\rangle = \delta_{(m'-m) \bmod N}, \quad (\text{E11})$$

where  $\delta_{n \bmod N}$  is the  $N$ -periodic Kronecker delta. A useful property of this setup is that the transformation between these two bases is identical to the discrete fast Fourier transformation as defined in most numerical libraries [63].

In order to adapt the Wigner function to this doubly discrete phase space, we start from the form (E5) found for action-angle variables, substituting directly  $p = \hbar l$  and replacing the limits of integration by the corresponding range of  $x$ ,

$$W_l(x) = \frac{1}{2\pi\hbar} \int_{-L/2}^{L/2} dx' e^{-2\pi i l x'} \psi^*([x-x'/2] \bmod L) \times \psi([x+x'/2] \bmod L). \quad (\text{E12})$$

Discretizing  $x$  as well leads to

$$W_{l,m} = \frac{1}{2\pi\hbar} \sum_{m'=-N/2}^{N/2-1} \exp\left(-2\pi i \frac{lm'}{N}\right) \left\langle m + \frac{m'}{2} \middle| \psi \right\rangle \times \left\langle \psi \middle| m - \frac{m'}{2} \right\rangle. \quad (\text{E13})$$

Under the sum, we switch to the momentum representation

$$W_{l,m} = \frac{1}{2\pi\hbar N} \sum_{m', l', l''=-N/2}^{N/2-1} \exp\left(2\pi i [l' - l''] \frac{m}{N}\right) \times \exp\left(2\pi i \left[\frac{l' + l''}{2} - l\right] \frac{m'}{N}\right) \langle l' | \psi \rangle \langle \psi | l'' \rangle, \quad (\text{E14})$$

and transform the momentum indices,  $k = l' + l''$ ,  $-N \leq k < N-1$ , and  $k' = l' - l''$ ,  $-N/2 \leq k' < N/2-1$ ,

$$\begin{aligned}
W_{l,m} = & \frac{1}{2\pi\hbar N} \sum_{k=-N}^{N-1} \sum_{k'=-N/2}^{N/2-1} \exp\left(2\pi i \frac{k'm}{N}\right) \\
& \times \sum_{m'=-N/2}^{N/2-1} \exp\left(2\pi i \left[\frac{k}{2}-l\right] \frac{m'}{N}\right) \left\langle \frac{k+k'}{2} \middle| \psi \right\rangle \\
& \times \left\langle \psi \middle| \frac{k-k'}{2} \right\rangle. \tag{E15}
\end{aligned}$$

The inverse transformation,  $l' = (k+k')/2$ ,  $l'' = (k-k')/2$ , shows that  $k$  and  $k'$  must have the same parity in order that  $l'$  and  $l''$  be integer, a consequence of switching to diagonal coordinates in a square lattice.

If  $k$  and  $k'$  are both *even*, the  $m'$  summation in Eq. (E15) reduces to a Kronecker delta that restricts  $k$ , giving

$$W_{l,m}^e = \frac{1}{2\pi\hbar} \sum_{\substack{l'=-N/2 \\ \text{even}}}^{N/2-1} \exp\left(2\pi i \frac{l'm}{N}\right) \left\langle l + \frac{l'}{2} \middle| \psi \right\rangle \left\langle \psi \middle| l - \frac{l'}{2} \right\rangle, \tag{E16}$$

in complete analogy to Eq. (E8). If they are both *odd*, say  $k = 2j + 1$ , the sum over  $m'$  no longer leads to a solution local in  $k$ . The result, after removing the remaining asymmetry in the boundary terms, is [64]

$$\sum_{m'=-N/2}^{N/2-1} \exp\left(2\pi i \left[l - j - \frac{1}{2}\right] \frac{m'}{N}\right) = \frac{\sin\left(\frac{N-1}{N} \left[l - j - \frac{1}{2}\right] \pi\right)}{\sin\left(\frac{1}{N} \left[l - j - \frac{1}{2}\right] \pi\right)}. \tag{E17}$$

By another renaming of indices it can be cast in the form

$$\begin{aligned}
W_{l,m}^o = & \frac{1}{2\pi\hbar} \sum_{\substack{l'=-N/2 \\ \text{odd}}}^{N/2-1} \exp\left(2\pi i \frac{l'm}{N}\right) \\
& \times \sum_{l''=l-N/2}^{l+N/2-1} \frac{\sin\left(\frac{N-1}{N} \left[l'' + \frac{1}{2}\right] \pi\right)}{\sin\left(\frac{1}{N} \left[l'' + \frac{1}{2}\right] \pi\right)} \\
& \times \left\langle l + \frac{l'}{2} - \left(l'' + \frac{1}{2}\right) \middle| \psi \right\rangle \left\langle \psi \middle| l - \frac{l'}{2} - \left(l'' + \frac{1}{2}\right) \right\rangle. \tag{E18}
\end{aligned}$$

This relation again shows a close similarity to the corresponding (odd- $l$ ) result for a cylindrical phase space, cf. Eq. (E8), i.e., there appears an additional summation parallel to the main diagonal of the momentum lattice, with an algebraically decaying kernel. In contrast to Eq. (E8), however, here the  $l''$  summation need not be truncated in a practical evaluation since it runs only over a single period of the momentum lattice (continued periodically, if required). In the limit  $N \rightarrow \infty$ , Eq. (E8) is recovered.

By the symplectic symmetry of the construction, see Eq. (E11), it is clear that an analogous derivation will yield expressions for the Wigner function in terms of the position-representation states  $\langle m | \psi \rangle$ , essentially identical to Eqs. (E16) and (E18). A generalization to nonpure states is readily achieved by replacing  $|\psi\rangle\langle\psi|$  with the density operator.

- 
- [1] D. J. Tannor and S. A. Rice, *Adv. Chem. Phys.* **90**, 441 (1988).  
[2] D. J. Tannor, *Nature (London)* **369**, 445 (1994).  
[3] See, e.g., T. H. Oosterkamp, L. P. Kouwenhoven, A. E. A. Koolen, N. C. van der Vaart, and C. J. P. M. Harmans, *Phys. Rev. Lett.* **78**, 1536 (1997), and references therein.  
[4] R. H. Blick, D. W. van der Weide, R. J. Haug, and K. Eberl, *Phys. Rev. Lett.* **81**, 689 (1998).  
[5] H. A. Kramers, *Collected Scientific Papers* (North-Holland, Amsterdam, 1956), p. 272; W. C. Henneberger, *Phys. Rev. Lett.* **21**, 838 (1958); W. Pauli and M. Fierz, *Nuovo Cimento* **15**, 167 (1938).  
[6] W. S. Truscott, *Phys. Rev. Lett.* **70**, 1900 (1993).  
[7] For a collection of recent articles see, e.g., *Chem. Phys.* **217**, 117 (1997), special issue, edited by W. Domcke, P. Hänggi, and D. Tannor.  
[8] For a collection of recent articles see, e.g., *Quantum Dynamics of Submicron Structures*, Vol. 291 of *NATO Advanced Studies Institute, Series E: Applied Sciences*, edited by H. A. Cerdeira, B. Kramer, and G. Schön (Kluwer, Dordrecht, 1995).  
[9] J. S. Howland, *Indiana Univ. Math. J.* **28**, 471 (1979).  
[10] K. Yajima, *J. Math. Soc. Jpn.* **29**, 729 (1979).  
[11] For a recent review see, e.g., P. Hänggi, in *Quantum Transport and Dissipation*, edited by T. Dittrich *et al.* (Wiley-VCH, Weinheim, 1998), p. 249.  
[12] F. Borgonovi and I. Guarneri, *J. Phys. A* **25**, 3239 (1992); *Phys. Rev. A* **48**, R2347 (1993).  
[13] P. Šeba, *Phys. Rev. E* **47**, 3870 (1993); P. Šeba and P. Gwinski, *ibid.* **50**, 3615 (1994).  
[14] I. Vorobeichik, R. Lefebvre, and N. Moiseyev, *Europhys. Lett.* **41**, 111 (1998); I. Vorobeichik and N. Moiseyev, *J. Phys. B* **31**, 645 (1998).  
[15] G. A. Luna-Acosta, G. Orellana-Rivadeneira, A. Mendoza-Galván, and C. Jung, *Chaos, Solitons Fractals* **12**, 349 (2001).  
[16] K. Takahashi and K. S. Ikeda, *Ann. Phys. (N.Y.)* **283**, 94 (2000).  
[17] U. Peskin and N. Moiseyev, *J. Chem. Phys.* **99**, 4590 (1993); *Phys. Rev. A* **49**, 3712 (1994).  
[18] N. Moiseyev, *J. Chem. Phys.* **101**, 9716 (1994).  
[19] T. Kovar and P. A. Martin, *J. Phys. A* **31**, 385 (1998).  
[20] A. Pimpale, S. Holloway, and R. J. Smith, *J. Phys. A* **24**, 3533 (1991).  
[21] G. Casati and L. Molinari, *Prog. Theor. Phys. Suppl.* **98**, 285 (1989).  
[22] M. Grifoni and P. Hänggi, *Phys. Rep.* **304**, 229 (1998).  
[23] U. Smilansky, in *Chaos and Quantum Physics*, Les Houches Lectures LII, edited by M.-J. Giannoni, A. Voros, and J. Zinn-Justin (North-Holland-Elsevier, Amsterdam, 1992), p. 371, and references therein.

- [24] C. Jung and T. H. Seligman, *Phys. Rep.* **285**, 77 (1997).
- [25] R. Blümel and W. P. Reinhardt, *Chaos in Atomic Physics* (Cambridge University Press, Cambridge, 1997).
- [26] F. F. Karney, *Physica D* **8**, 360 (1983).
- [27] O. Legrand and D. Sornette, *Europhys. Lett.* **11**, 583 (1990).
- [28] J. D. Meiss and E. Ott, *Phys. Rev. Lett.* **55**, 2741 (1985).
- [29] P. J. Richens and M. V. Berry, *Physica D* **2**, 495 (1981).
- [30] J. H. Hannay and R. J. McCraw, *J. Phys. A* **23**, 887 (1990).
- [31] C. Lipp and C. Jung, *J. Phys. A* **28**, 6887 (1995).
- [32] J. L. Mateos and J. V. José, *Physica A* **257**, 434 (1998); J. L. Mateos, *Phys. Lett. A* **256**, 113 (1999).
- [33] T. Dittrich, E. Doron, and U. Smilansky, *Physica B* **179**, 1 (1992); *J. Phys. A* **27**, 79 (1994).
- [34] C. Jung, T. Tél, and E. Ziemniak, *Chaos* **3**, 555 (1993).
- [35] A. J. Lichtenberg and M. A. Lieberman, *Regular and Stochastic Motion*, Applied Mathematical Sciences Vol. 38 (Springer, New York, 1983), Chap. 6.1b.
- [36] Ref. [35], Chap. 3.4.
- [37] M. Henseler, T. Dittrich, and K. Richter, *Europhys. Lett.* **49**, 289 (2000).
- [38] B. Birnir, B. Galdrikian, R. Grauer, and M. Sherwin, *Phys. Rev. B* **47**, 6795 (1993); W. Chism, T. Timberlake, and L. E. Reichl, *Phys. Rev. E* **58**, 1713 (1998).
- [39] M. Robnik and M. V. Berry, *J. Phys. A* **18**, 1361 (1985).
- [40] J. J. Sakurai, *Modern Quantum Mechanics* (revised edition) (Addison-Wesley, Reading, 1994).
- [41] R. G. Newton, *Scattering Theory of Waves and Particles*, 2nd ed. (Springer, New York, 1982).
- [42] T. Millack, *J. Phys. B* **23**, 1693 (1990).
- [43] D. S. Saraga and M. Sassoli de Bianchi, *Helv. Phys. Acta* **70**, 751 (1997).
- [44] P. A. Martin and M. Sassoli de Bianchi, *J. Phys. A* **28**, 2403 (1995).
- [45] M. Henseler, Ph.D. thesis, Technical University of Dresden, 1999.
- [46] A. D. Stone and A. Szafer, *IBM J. Res. Dev.* **32**, 384 (1988).
- [47] H. Friedrich, *Theoretical Atomic Physics* (Springer, Berlin, 1990).
- [48] A. Weingartshofer and C. Jung, in *Multiphoton Ionization of Atoms*, edited by S. L. Chin and P. Lambropoulos (Academic Press, Toronto, 1984), p. 155.
- [49] F. H. Faisal, *Theory of Multiphoton Processes* (Plenum, New York, 1987).
- [50] M. Pont, N. R. Walet, M. Gavrilu, and C. W. McCurdy, *Phys. Rev. Lett.* **61**, 939 (1988); M. Pont, N. R. Walet, and M. Gavrilu, *Phys. Rev. A* **41**, 477 (1990).
- [51] F. Grossmann, T. Dittrich, P. Jung, and P. Hänggi, *Phys. Rev. Lett.* **67**, 516 (1991).
- [52] R. Blümel and U. Smilansky, *Phys. Rev. Lett.* **64**, 241 (1990).
- [53] N. L. Balazs and A. Voros, *Ann. Phys. (N.Y.)* **199**, 123 (1990).
- [54] H.U. Baranger, R.A. Jalabert, and A.D. Stone, *Chaos* **3**, 665 (1993).
- [55] For recent reviews see, e.g., K. Richter, *Semiclassical Theory of Mesoscopic Quantum Systems* (Springer, Berlin, 2000); R. A. Jalabert, in *New Directions in Quantum Chaos*, edited by G. Casati, I. Guarneri, and U. Smilansky (IOS Press, Amsterdam, 2000).
- [56] M. Wagner and W. Zwerger, *Phys. Rev. B* **55**, R10 217 (1997).
- [57] M. Wagner, *Phys. Rev. B* **49**, 16 544 (1994); *Phys. Rev. A* **51**, 798 (1995).
- [58] M. V. Berry, *Philos. Trans. R. Soc. London, Ser. A* **287**, 237 (1977).
- [59] N. L. Balazs and A. Voros, *Europhys. Lett.* **4**, 1089 (1987); *Ann. Phys. (N.Y.)* **190**, 1 (1989).
- [60] M. Saraceno, *Ann. Phys. (N.Y.)* **199**, 37 (1990).
- [61] J. H. Hannay and M. V. Berry, *Physica D* **1**, 267 (1980).
- [62] D. Galetti and A. F. R. de Toledo Piza, *Physica A* **149**, 267 (1988); **186**, 513 (1992).
- [63] See, e.g., *NAG Fortran Library*, Mark 18 (The Numerical algorithm Group Ltd., Oxford, 1997).
- [64] I. S. Gradshteyn and I. M. Ryzhik, *Table of Integrals, Series and Products* (Academic Press, San Diego, 1965), formula 1.342/2.